Strength modeling of Al-alloy sheet self-piercing riveting considering different failure modes

Yahui Liu (allensmith@sjtu.edu.cn)
Shanghai Jiao Tong University https://orcid.org/0000-0002-5371-6091
Zhiwang Zhu
Huipeng Yu
Jun Wang

Research Article

Keywords: Self-piercing riveting (SPR), aluminum alloy sheet, rivet flaring, riveting strength model, industrial internet of things (IIoT)

Posted Date: October 4th, 2022

DOI: https://doi.org/10.21203/rs.3.rs-2052846/v1

Strength modeling of Al-alloy sheet self-piercing riveting considering different failure modes

Yahui Liu [a, b,*], Zhiwang Zhu [a], Huipeng Yu [a], Jun Wang [a, b, c,*]

a. School of Materials Science and Engineering, Shanghai Jiao Tong University, No. 800, Dongchuan Road, Shanghai 200240, China

b. Shanghai Key Laboratory of Advanced High-temperature Materials and Precision Forming, Shanghai Jiao Tong University, 800 Dongchuan Road, Minhang District, Shanghai, 200240, China

c. State Key Laboratory of Metal Matrix Composites, Shanghai Jiao Tong University, 800 Dongchuan Road, Minhang District, Shanghai, 200240, China

* Corresponding author. E-mail: allensmith@sjtu.edu.cn (Yahui Liu, ORCID: 0000-0002-5371-6091), junwang@sjtu.edu.cn (Jun Wang).

Abstract

Self-piercing riveting (SPR) has been widely utilized to connect metal components in industry, and the mechanical properties of final product depend on the strength of SPR joint which is experimentally measured through cross-tension and lap-shear tests. These tests are destructive and the tested strength of specimen is not directly related to the actual strength of the SPR product. In this study, the SPR process of aluminum alloy sheet was investigated and the general empirical model of SPR strength was established by comprehensively considering the factors including of the geometric dimensions of components and die, the material properties of rivet and sheet, and the load - stroke curve of punch. The calculated strength values of 4 group of SPR specimens were verified by the experimentally measured results. All

calculation errors are lower than 8%. An industrial internet of things (IIoT) was developed to automatically realize the data transmission and strength calculation of the SPR process.

Keywords

Self-piercing riveting (SPR); aluminum alloy sheet; rivet flaring; riveting strength model; industrial internet of things (IIoT)

1. Introduction

Self-piercing riveting (SPR) is one of the high-efficiency processes to connect sheet materials, in which a rivet is pushed into the stacked sheets in a certain direction under the force of a punch [1-3]. At the same time, the deformed metal is formed into a button shape with a mold assembled on the other side of the sheet. In practice, the number of sheets prepared for SPR can be more than double layers. As an instance, three layers of Al alloy sheets connected via SPR process were studied by Han, et al. [4]. Moreover, SPR process is extremely suitable to connect sheets that are made of similar or dissimilar materials [5]. Typically, SPR is successfully utilized to connect low-strength metals such aluminum alloy and copper alloy. For example, Calabrese, et al. [6] studied the SPR of AA6111 sheet and obtained the failure map for net-tension and pull-out mechanisms. He, et al. [7] compared the joint performances of the SPR of copper alloy H62 sheets and the SPR of Al-to-Cu sheets. Besides, high-strength materials can also be connected via SPR process. Xie, et al. [8] investigated the cross-tension strength of the SPRed cold formed steel sheets. Zhao, et al. [9] reported the SPR process of titanium alloy TA1 sheet. Additionally, SPR process is applied to connect composite sheet. The SPR of the carbon fiber reinforced polymer composite sheet was studied by Rao, et al. [10]. And the glass fiber reinforced thermoplastic composite sheet was studied by Gay, et al. [11]. The sheet subjected to SPR may also be covered with surface coating, such as the corrosion resistance coating and electrical insulation coating reported by Han and Chrysanthou [12]. The candidates for rivet material can be different according to the sheet material. the steel HSLA350 rivet was utilized to connect aluminum alloy AA6111 sheets by Han, Chrysanthou and Young [4]. While aluminum alloy rivets made of 6082-T6, 7108-T5, and 7278-T6 were utilized by Hoang, et al. [13] to aluminum alloy 6060 sheets in three different tempers (temper W, temper T4, and temper T6). The forming of SPR button depends on the die cavity which also has different designs. Karathanasopoulos, et al. [14] compared the influences of different die tip design on the feasibility and quality of the SPR joints.

The broad application of SPR is due to the its following advantages: the wide range of material applicability even for the materials with poor weldability, high forming efficiency, material saving (no need for pre-drilling, no remnant), energy saving (no need for preheating), environmental friendly (no pollution emission), and lightweight manufacturing. SPR also offers more advantages over other bonding processes, such as resistance spot welding (RSW). Sun and Khaleel [15] found that SPR joints of metal sheets had better dynamic impact strength fatigue strength than the joint of resistance spot welding. Also, Sun, et al. [16]found that the fatigue strength of SPR joints was better than the joint of resistance spot welding. Currently, some researches combine SPR process with other bonding methods to improve the interlock strength of the joints. Ma, et al. [17] employed the friction self-piercing riveting (F-SPR) to bond low ductility materials. Ma, et al. [18] also studied the bonding strength of F-SPRed AA7075-T6 aluminum alloy joints. Yang, et al. [19] investigated the hybrid process of F-SPR and adhesive bonding of Al7075-T6 alloy sheets where the adhesive was utilized for lubrication.

Yang, et al. [20] studied the Al-to-Mg sheet F-SPR and optimized the design of bottom die. Ma, et al. [21] found that the rivet orientation significantly affect the quality of Al-to-Mg F-SPR joint. Ying, et al. [22] studied the thermal self-piercing riveting (T-SPR) of AA7075-to-T6 sheets and the failure modes of the joints. Han, et al. [23] developed an innovative SPR to connect the sheets made of glass fiber reinforced polymer (GFRP). Jiang, et al. [24] studied the Electromagnetic self-piercing riveting (E-SPR) of CFRP-to-Al and steel-to-Al sheets and found the structure of rivet had significant influences on the quality. All these researches have extended the applications of SPR and improved the connecting quality of joints.

The major application fields of SPR include automotive industry (e.g. structural components), electrical industry (e.g. busbar support), aircraft industry and so on. Due to the demand for lightweighting of automobiles, new techniques have emerged in the field of SPR. Danyo [25] highlighted that SPR is one of the key jointing methods in vehicle. The current tendencies of the SPR applications in vehicle body include the connection of dissimilar materials of metal and composite, and the jointing of high-strength metal and low-ductility metal. Wang, et al. [26] remarked that the SPR of metal and composites sheets has become a major part of the new jointing techniques. Karim, et al. [27] also pointed out that SPR is more suitable for bonding dissimilar materials than other conventional jointing processes. However, there are also challenges for the industrial applications of SPR recently including of the quality prediction on the automatic production line, the high-efficiency optimization of the tool design for certain SPR process, and the development of new SPR process. Many literatures focus on the quality prediction of SPR joints, and parts of the issues include the metal deformation during SPR process, the mechanical properties of SPR joint, the modeling of joint strength and so on.

Kyoung-Yun Kim, et al. [28] discussed the challenges facing SPR in the quality prediction, and compared the main methods of quality prediction, including of experimental test, finite element method (FEM), numerical equation model, and data-driven model. Notably, to establish a robust quality prediction model for SPR is still a hard bone for engineers and researchers because many unknown variables in the changing manufacturing scenes result in the individual differences of SPR joints. Those unknown variables could be one or more of the following aspects: the inhomogeneous properties, the internal defects as the nature of material, the uneven deformation of rivet during operation, the pressure fluctuations of forming tools, the wear of bottom die and so on. Actually, a single quality prediction method is insufficient to cover all the concerns in practice. Nevertheless, the it is possible to establish a sound model to predict SPR quality by controlling for variables, and the main steps could be summarized as follows: (a) analyze the SPR processing, (b) selecting the key variables affecting joint quality, (c) selecting the most suitable quality prediction model and establishing the model, (d) verifying the quality model and improve it.

SPR process of metal sheets is a typical cold forming procedure, which is divided into three deformation stages by Porcaro, et al. [29]: (a) under the pressure of punch, the rivet pierces through the head-side sheet materials without significant plastic deformation; (b) the rivet flaring increases rapidly and the bottom sheet metal starts to fill the die cavity. Generally, the stacked sheets and bottom die are fixed during the processing. SPR process has been illustrated in other studies. The aluminum-to-steel SPR with a steel rivet was divided into three stages including of clamping, riveting and mold opening by Lou, et al. [30]. The A6060-to-A6060 sheet SPR with a high-strength steel rivet was divided into four stages by Porcaro, Hanssen, Langseth and Aalberg [29] in terms of clamping, piercing, flaring and release of punch. The SPR process was also divided into four stages named clamping, piercing, flaring and release of punch by Su, et al. [31], as well as Zhang, et al. [32]. The SPR of steel sheet was divided into six stages by Yan, et al. [33] including of die clamping, punch clamping, punch expert pressure, rivet piercing, deformation, and forming. All the demonstrations on the procedure of SPR in those literatures paid attentions to the tool motion and the material deformation, especially the rivet piercing through the stacked sheets and flaring in the metal sheet under the compression of punch. The rivet joint is a final representation of the component deformation, most of which is recorded in the load-displacement curve of punch and the final shape of the rivet joint. It's necessary to discuss the factors affecting the component deformation, joint strength and joint defects, which are expected to help improve the quality of SPR product.

The performances of SPR joint include strength index (e.g. cross-tension strength and lap-shear strength), fatigue life, fretting wear, heat resistance and corrosive resistance. The cross-tension strength and lap-shear strength of SPR joint are the maximum force value measured in the cross-tension test and lap-shear test, respectively, which are widely utilized in industrial practice. The fatigue behaviors of SPR joint are usually investigated by using the specimens with lap-shear type, cross-tension type, U-shaped type, and coach-peel type. The cross-tension specimen of cold form steel sheet was utilized by Xie, et al. [34] to study the tensile strength of SPR. The finite element models of cross-tension, lap-shear, and coach-peel specimens were built by Kang and Kim [35] to study the fatigue strength of SPRed Al5052 sheet. The specimens with lap-shear type and U-shaped type were utilized by Wu, et al. [36] in order to investigate the fatigue behaviors of SPRed AA6111-T4. The lap-shear and coach-peel specimens were utilized by Presse, et al. [37] to estimate the fatigue life of SPRed Al-to-steel joint. Those specimens can also be used to study the wear behaviors of SPR joint. The wear of lap-shear specimen at the interface between sheet and rivet was studied by Chen, et al. [38]. Kotadia, et al. [39] found that the corrosion condition has significant influences on the failure of the joint of the coated Al-to-steel sheet SPR. All the above tests are destructive experiments which cannot be directly applied to the actual SPR product. Hence, a theoretical calculation model is useful to predict the quality of SPR joints in industrial practice. However, the robustness of the strength model is first issue that should be considered when calculating the strength of SPR joints.

In order to establish a theoretical model of the strength of metal SPR joint, it is necessary to analyze which parameters have a significant effect on the strength of SPR joint. Parameters related to the SPR strength can be divided into the following three categories: (a) the material properties of sheet and rivet (e.g. density, Young's module, yield strength and hardness), (b) the geometric dimensions of components (e.g. the thickness of stacked sheet, the diameter and length of rivet, the rivet flaring, the diameter and depth die cavity) [40], (c) the processing parameters (e.g. the load - stroke curve of punch, riveting direction). Zhao, et al. [41] reported that increasing the thickness of sheet in a certain range can increase the fatigue life of SPR joint and decrease the fretting wear at the interface between stacked sheets. Haque and Durandet [42] studied the steel-to-steel SPR and obtained the conclusion that increasing the diameter of rivet can improve the strength of SPR joint under impact load testing. Moreover, Sun and Khaleel [43] found that the flaring shape of rivet dominates the interlock of stacked sheets, so SPR joints with larger rivet flaring have higher static strength. The load-stroke curve of punch can record the details of materials deformation during SPR process, which was utilized to quantify the rivet flaring by Sun and Khaleel [44]. The rivet flaring is one of the most important factors due to the interlock strength increases with the value of rivet flaring increasing. Besides, the coating of sheet is also an important factors affecting the fractional statement and the joint strength, as reported by Karim, et al. [45].

The methods of SPR strength modeling generally include numerical simulation (e,g. FEM) [46-48], theoretical analysis method, and data-driven modeling. Firstly, numerical simulation is believed an effective way to analyze the time-evolution history of displacement, stress, and strain field in the processing of cold metal deformation like SPR. From simulation result, it is easily to obtain the deformation profile of rivet and stacked sheet during SPR process and to directly measure the value of rivet flaring. The simulation results can also help to draw the load-stroke curve of punch. Many studies use numerical simulation to build two-dimension (2D) or three-dimension (3D) model of the SPR process. Using software LS-DYNA, Hoang, Porcaro, Langseth and Hanssen [13] successfully applied a 2D axisymmetric model to the SPR of aluminum alloy sheet with aluminum rivets. A 3D model of the Mg-to-Al SPR process was established through ABAQUS by Moraes, et al. [49], and it was found that the strain hardening caused by SPR process is one of the main contributions for the joint strength. Du, et al. [50] studied the Al-to-steel sheet SPR process by using a 2D axisymmetric model established through LS-DYNA based on radaptivity method. Modeling the SPR process of Al sheet with a steel rivet was studied by Casalino, et al. [51], and the simulation results were validated by experimental data. Carandente, et al. [52] proposed a 2D axisymmetric FE model to analyze the thermo-mechanical behaviors caused by friction during Al sheet SPR process. Other researchers studied the structure strength of SPR joint by numerical simulation in order to predict the mechanical behaviors and quality of SPR joints. Lukas Potgorschek [53] improved the conventional 2D FE model of SPR process and obtained an accurate force-displacement curve of punch. Hönsch, et al. [54] proposed a 2D FE model and a 3D FE model to simulate the SPR processing and the tension test of joint, respectively, and the simulation results of the joint behaviors were consistent with experiment results. However, numerical simulation method is not only time-consume in preparing the stringent input and complex settings of the model, but also quite inaccurate because it neglects the material differences and dimensional deviation of component to simplify the calculation model. Weighting the advantages and disadvantages of numerical simulation, it is preferable to apply numerical simulation to product design or process research rather than quality control on production line.

Theoretical analysis is a candidate method for evaluating the strength of SPR joints by using explicit empirical equations instead of complicated calculation based on finite element model. For example, Sun and Khaleel [43] established two estimators to calculate the cross-tension strength of SPR joints cracked in failure mode I (rivet tail pullout) and failure mode II (rivet head pullout) respectively, and the failure mode of SPR joints can be predicted by comparing the calculated values of cross-tension strength, where only 3 empirical coefficients and 3 material parameters were involved in each estimator. However, two important material parameters in the estimator of failure mode I, diameter of clinched portion of rivet tail (D_c) and effective material thickness on tail side (t_{eff}), were obtained by destructive examination. Haque, et al. [55] developed a mathematical model to calculate rivet flaring (Δd) instead of using destructive examination. Further, Haque and Durandet [42] associated the parameters D_c and t_{eff}

with the rivet flaring and directly calculated the cross-tension strength of SPR joint, where the input variables involved empirical coefficient, punch displacement, and the design dimensions of rivet, sheet and die cavity. They also developed a formula to calculate lap-shear strength from the cross-tension strength of the steel-to-steel sheet SPR joint. Kim, et al. [56] developed the analytical strength estimators for SPR joints for the lap-shear and the cross-tension modes, where the numerical simulation was utilized to reveal the mechanical responses of the rivet and sheets during the SPR process and the lap-shear and the cross-tension tests. The authors tried to develop the strength estimators with using the calculated material properties rather than empirical coefficients in order to simplify the calculation procedure. In their strength models, the lap-shear strength is the product of the four important parameters are the tensile strength of sheet metal, the effective contact thickness and diameter (geometric parameters), which are also used in previous literatures, such as Sun and Khaleel [43] and Haque, Williams, Blacket and Durandet [55]. However, a reference coefficient representing a ratio to uniform elongation was also involved in their strength models. The prediction on the failure mode of rivet joint is another important issue, which is related to the mechanical performance of the SPR joint. Commonly, the failure mode is the results of the competency between the rivet head pullout and rivet tail pullout. Therefore, the failure mode of a SPR joint can be curtained by comparing the strength index of the rivet head pullout and rivet tail pullout, after the strength indexes been calculated. Porcaro, et al. [57] studied the Eurocode 9 and reported the equation to calculate the resistance force of the rivet head pullout and rivet tail pullout in cross-tension test, respectively, where the resistance force of SPR joint is the product of the ultimate tensile strength of material and geometric dimensions of rivet parts. Calabrese, Bonaccorsi, Proverbio, Di Bella and

Borsellino [6] improved the work of Porcaro, Hanssen, Langseth and Aalberg [57] and proposed an equation to predict the failure mode of lap-shear SPR joint.

These studies focused on the development of the cross-tension strength model of the SPR joint based on rivet flaring, but the lap-shear strength models of failure mode I and II have not been involved. Considering the various SPR processes and joint failure modes in actual situations, it is necessary to improve the established strength models of SPR joint to extend their applications, especially considering the different failure modes in the lap-shear test and the cross-tension test of SPR joint.

This work attempts to develop a general model to predict the strengths and failure modes of the Al-to-Al sheet SPR joints with one steel rivet, where the strengths include lap-shear strength and cross-tension strength, and the failure modes includes the rivet tail pullout and rivet head pullout. It is also possible to calculate the strengths based on their relationships in mathematic when one of the strengths is known. The destructive tests of cross-tension and lap-shear specimens were conducted to verify the prediction results which contained the joint strength and the joint failure mode. Furthermore, the established SPR strength models were embedded in an industrial internet of things (IIoT) to in line monitor the connection quality of SPR product.

2. Experiment method

2.1. SPR process of aluminum alloy sheet

In present study, two layers of Al alloy sheets are stacked and connected with a steel rivet by self-piercing riveting process. The schematic diagram of the SPR mold assemble is shown in Fig. 1. The material of Al alloy sheets is A6063-T5, and the steel rivet material is 37Cr4 steel. The chemical compositions of A6063-T5 and 37Cr4 are shown in Table 1 and Table 2, respectively. The mechanical properties of A6063-T5 and 37Cr4 are shown in Table 3. The Al alloy sheet under consideration contains two types: (a) type 1 is one-side coated Al sheet, and (b) type 2 is double-side coated sheet. Compared with the Al alloy sheet and the steel rivet, the insulation coating can be omitted in the study due to its small thickness and low mechanical strength.

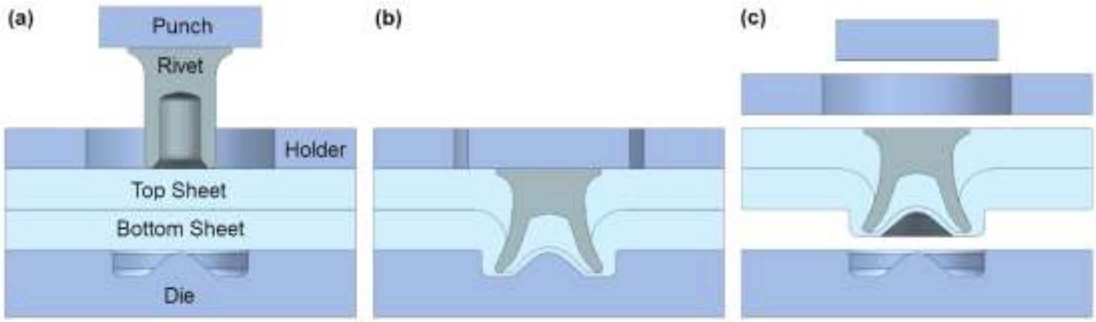

Fig. 1. The SPR schematic diagram of aluminum alloy sheet: (a) preparation, (b) forming, (c) demolding.

Table 1 Chemical compositions of Aluminum 6063-T5.

Element	Al	Mg	Si	Cr	Mn	Ti	Cu	Zn	Fe
Weight/%	97.5	0.45-0.9	0.2-0.6	≤0.1	≤0.1	≤0.1	≤0.1	≤0.1	≤0.35

Table 2 Chemical compositions of 37Cr4 steel.

Element	C	Si	Mn	P	S	Cr
Weight/%	0.34 - 0.41	≤0.4	0.6 - 0.9	≤ 0.025	≤0.035	0.9 - 1.2

Table 3 The mechanical properties of Al alloy 6063-T5 and 37Cr4 steel.

Properties	Unit	6063-T5	37Cr4
Density	g/cm^3	2.7	7.8
Poisson's Ratio	-	0.33	0.29
Modulus of Elasticity	GPa	68.9	190
Shear Modulus	GPa	25.8	73
Tensile Yield Strength	MPa	145	630
Ultimate Tensile Strength	MPa	186	590
Elongation at Break	%	12	13
Brinell Hardness	-	60	235

The SPR device used for the Al sheet riveting is shown in Fig. 2. The bottom die is fixed on the anvil to form the metal into a button, and the punch is placed along horizontal direction to provide a push force for each riveting process. The rivets are beforehand prepared in a chain in order to automatically supply rivet for the SPR. An infra-red inspection device has been equipped to detect whether a steel rivet is already placed on the right position in each SPR process. Besides, an automatic feeding system is equipped on the production line to keep supplying the Al alloy sheet.

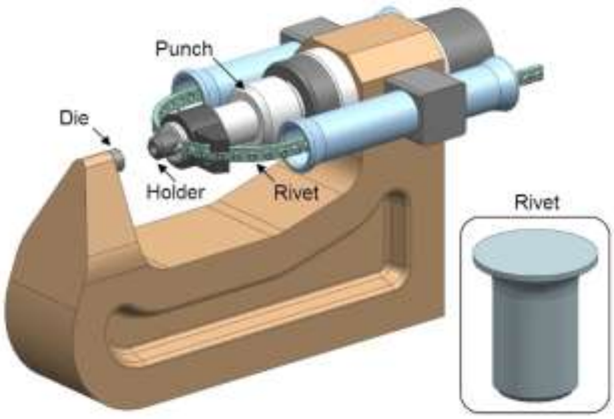

Fig. 2. The SPR device utilized for the Al sheet riveting.

2.2. IIoT in SPR production line

The SPR of Al alloy sheet is a procedure of cold metal deformation where a rivet is pressed into the two or multiple layers of sheets under punch pushing. The load - stroke curve of the punch is important data to determine the details of rivet deformation. For example, He, et al. [58] made use of the punch stroke to calculate the rivet flaring. No doubt, The rivet flaring is the primary factor that dominates the interlock of the stacked sheets and the strength of SPR joint, as reported by Hoang, et al. [59]. To obtain the load-displacement curve of each SPR process, an IIoT system was constructed based on hardware and software. The hardware the

IIoT makes use of a displacement sensor assembled on the side of the punch to measure the displacement of the punch and a pressure sensor amounted on the hydraulic drive station of the punch to measure the pressure change of the punch. Both the pressure sensor and displacement sensor have been adjusted to realize the synchronicity of the data acquisition. An analog-to-digital (A/D) card was utilized to convert the collected pressure-dislocation data from the analog signal to the digital signal. Afterwards, the digital signals of the displacement and pressure were transmitted to the software of the IIoT system aiming to sequentially complete the data processing and the results uploading, including the calculation of SPR joint strength and the uploading of calculation results to online database. The software of the IIoT is installed on a local industrial computer.

Regarding of the automatic SPR production line (see Fig. 2), the time duration of each SPR process in practice is limited in 3 seconds, and the time interval between two SPR processes is limited in 8 seconds. The IIoT system has the capability to catch the pressure-dislocation data of each SPR process in real time (3 seconds) and rapidly complete the relevant calculation before the start of the next SPR process. The data sampling frequency of the displacement sensor and the pressure sensor is set as 1000Hz. The raw data of the IIoT system is saved on the local industrial computer.

2.3. Destructive test of SPR joint

The monitored strength indexes of each SPR joint generally include the cross-tension strength and lap-shear strength. In order to determine whether the predicted strength of each SPR joint meets the quality requirements, a standard strength value is required as a reference. The standard strength value of the cross-tension strength and lap-shear strength were directly measured by conducting a series of deconstructive tests with SPR joint specimens, as shown in Fig. 3.

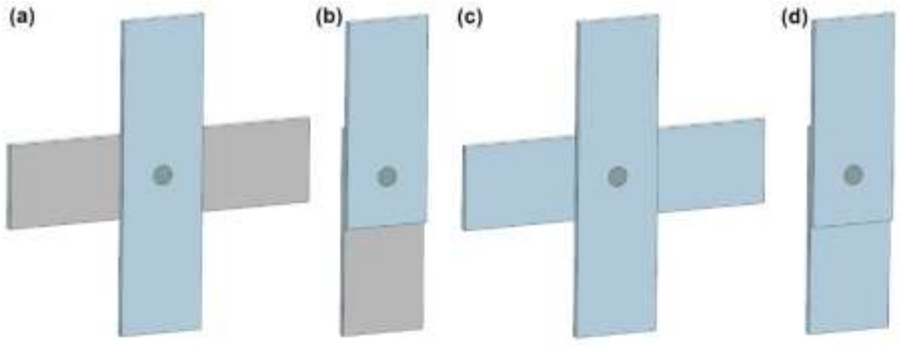

Fig. 3. The SPR specimens of destructive tests: (a) cross-tension specimen of group 1, (b) lip-shear specimen of group 1, (c) cross-tension specimen of group 3, and (d) lip-shear specimen of group 4.

In this study, the SPRed specimens for destructive test were divided into four groups: (a) group 1 is the sheet type 2 to sheet type 1 cross-tension specimen, (b) group 2 is the sheet type 2 to sheet type 1 lap-shear specimen, (c) group 3 is the sheet type 2 to sheet type 2 cross-tension specimen, (d) group 4 is the sheet type 2 to sheet type 2 lap-shear specimen. The type 1 is one-side coated sheet, and type 2 is double-side coated sheet. The cross-section views of the SPR joints in the four groups were observed by using an optical microscope Olympus BX51M and a scanning electron microscope (SEM) VEGA 3.

2.4. FE model of SPR

To analyze the metal deformation in SPR, numerical simulation was conducted by using a 2-dimensional (2D) finite element (FE) model via software ABAQUS, as shown in Fig. 4. The 2D FE model involved the rigid tools (punch, holder, and die), and the deformable components (rivet, top sheet and bottom sheet). The material properties of the rivet, the top sheet and the bottom sheet were set as shown in Table 1. The dimensions of the tools and the deformable components were the actual size value of relevant parts. The mass reference point of the punch was applied a velocity of 0.1 m/s on, and the mass reference point of the holder was applied a holding force of 100N. The degree of freedom of the bottom die was all fixed. The friction factors between tools and components were set as follows: 0.2 at the interface between steel rivet and Al alloy sheets, 0.22 at the interface between the Al alloy sheets, 0.2 at the interface between the tools and the Al alloy sheets, 0.2 at the interface between the tools and the rivet. The element type of rivet model is hybrid of rectangle and triangle, and the element type of sheets is rectangle. The element type of the deformable body in the FE model is quadrilateral element. The element of the top sheet is finer than that of the bottom sheet in order to reduce the impaction of large distortion in the top sheet on the computation convergence. The coating on the alloy sheet were not considered in the FE model.

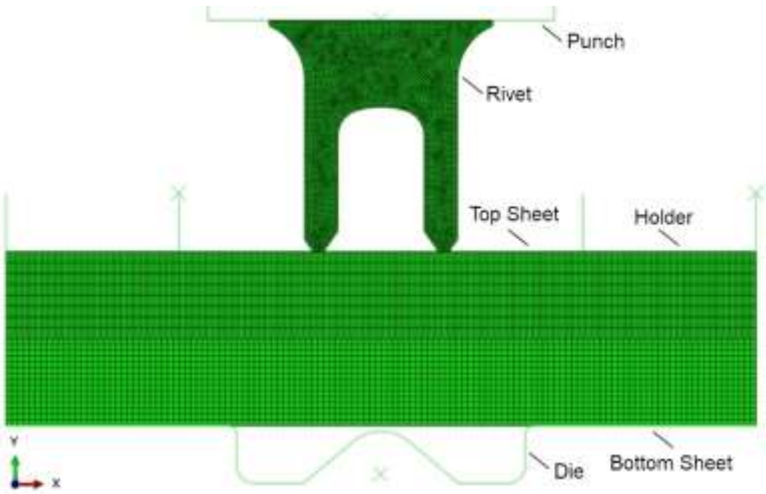

Fig. 4. The 2D axis symmetric FE model of SPR for the Al sheet and steel rivet.

3. Results and discussions

3.1. SPR simulation results

In investigating the procedure to fabricate a SPR joint of metal sheets in present industrial production line, it is common sense to pay attentions to the metal deformation details which reflect essential characteristics of the SPR process. In practice, the methods to sufficient the requirement generally include experimental metallography observation and the numerical simulation, both of which were coupled with the section view of SPR joint. The former method provides a clear perspective of SPR joint under microscope view field, even though the preparation of the specimen cross-section is time-consume and cost-expensive. As the alternative method, numerical simulation performs more efficiently in providing the details of continuous deformation during a SPR procedure, as shown in Fig. 5. The simulation results of the 2D FE model clearly presents the metal deformation of rivet, top sheet and bottom sheet at different punch stroke. With the steel rivet being driven into the op Al alloy sheet with a thickness of 3mm, the predicted Mises effective stress in the rivet tail continuously is clamming up to a high value above 800 MPa, which directly force the rivet tail to flare. The simultaneous deformation occurs in the top alloy sheet that partial material of the top sheet is pierced away and trapped in the hollow cavity of the rivet tail. When the punch stroke reaches 65%, the rivet tail already pierces through the top sheet and drives the partial metal of the bottom sheet to fill the cylinder mold cavity, as shown in Fig. 5(d). With the punch stroke increasing, the rivet flaring increases and the bottom sheet tends to fill fully the entire mold cavity. Due to the complexity of metal flowing in the mold cavity, the compress load of the punch against the metal deformation increase rapidly. A cone structure in the bottom mold is designed to promote the rivet flaring and to achieve a fully filled button. A final action of the punch is to stamp on the top sheet to avoid sheet rebound and to reduce sheet gap, leading to the punch load to reach its maximum value. Moreover, no significant deformation occurs in the rivet heat throughout the SPR process.

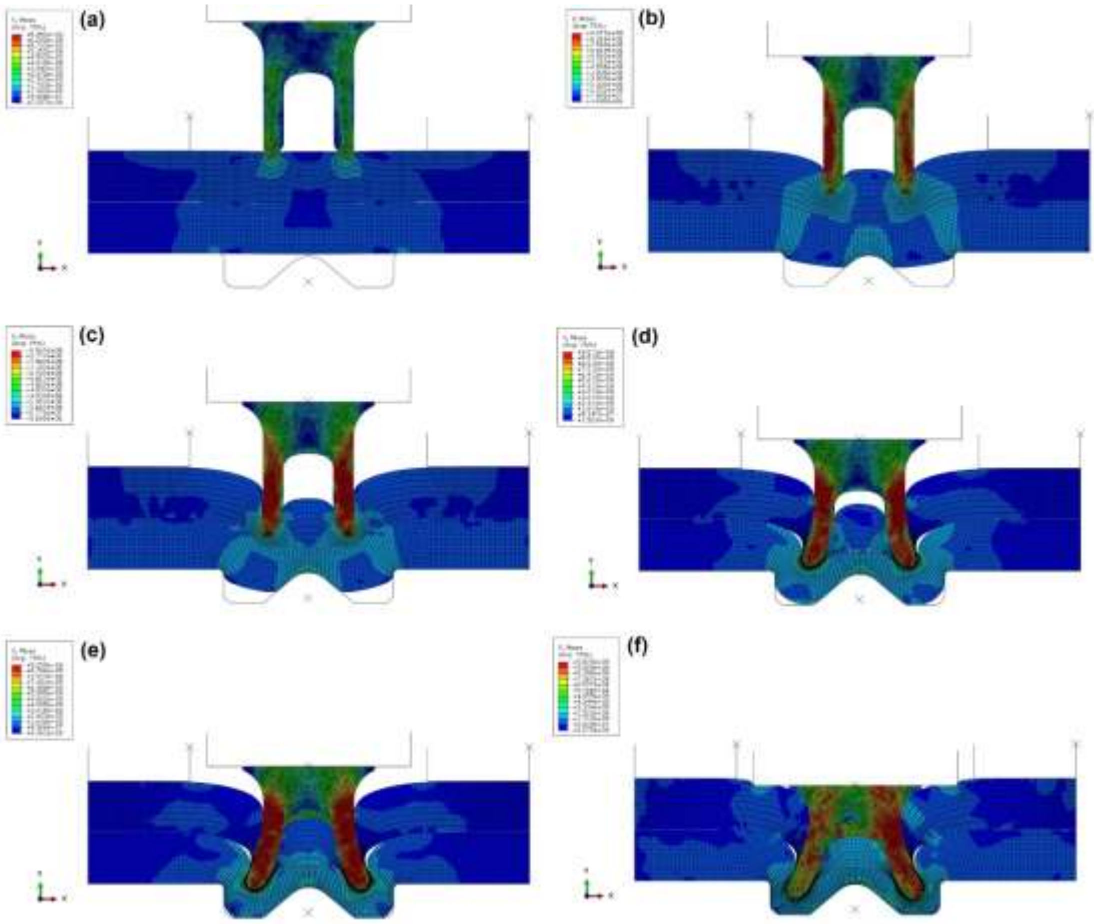

Fig. 5. FE simulation results of Mises stress at the different punch stroke: (a) 5%, (b) 25%, (c) 45%, (d) 65%, (e) 85%, and (f) 100%.

Furthermore, the predicted displacement distribution in Fig.6 suggests the metal flowing during the SPR process. The maximum horizontal flowing of the sheet metal along X axis direction is caused by the rivet piercing and the rivet flaring results in the tail deforming in the opposite direction, which reveals the main principle of the SPR bounding and the generation of the connection strength. In the vertical direction, the rivet travels a long distance through the two metal sheet before it struggles to reach the final position. This travel can be divided into two stages: (1) stage I of the rivet starts from it contacting the top sheet and ends with the rivet tail going into the mold cavity; (2) stage II is the rivet flaring procedure. However, to define the precise demarcation point of the two stages is an engineering problem for the various factors in the real SPR process, such as the hardness of materials. Above all, the rivet flaring is one of the factors dominating the connecting the stacked sheets in SPR process.

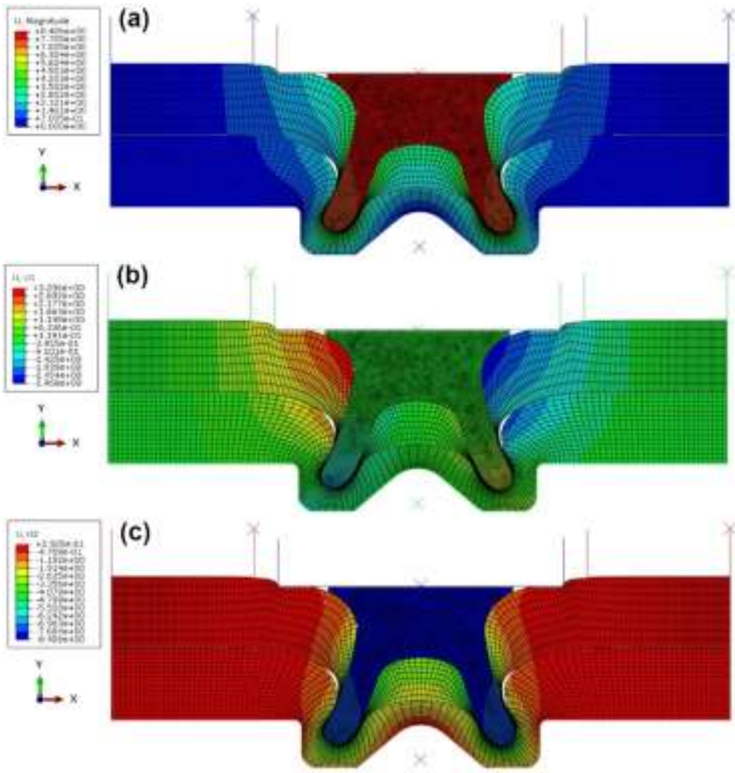

Fig. 6. The predicted displacement field of SPR joint in (a) total magnitude, (b) X axis direction, and (c) Y axis direction.

3.2. SPR experiment results

More details of the metal deformation in SPR process can be found in the metallographic picture of the joint cross-section, as shown in Fig. 7. As discussed in section 3.1, the rivet flaring is one of the critical factor that dominated the connection strength of SPR joint. The measured rivet flaring of the group 1 - 4 is 0.69±0.11 mm, 0.65±0.13 mm, 0.73±0.14 mm, and 0.62±0.15 mm, respectively. The differences between those rivet flaring is caused by the essential material properties and the key dimensional deviations of the components. The differences of the material properties commonly includes the density, Young's modules, Poisson rate, yield strength and hardness, which have significant contribution to the rivet flaring deformation. Especially, Haque and Durandet [42] reported that a small change of yield strength of sheet will largely change the metal deformation in SPR process. The dimensional deviation of each SPR process is basically the rivet diameter, sheet thickness, and mold cavity size (depth and diameter). For example, the real rivet is not perfectly axisymmetric, which will cause a small difference of the rivet flaring in the metallography. More details of the deformed rivet and Al alloy sheet are shown in Fig. 8. No crack or folds were found at the interface between the rivet and the Al alloy sheet.

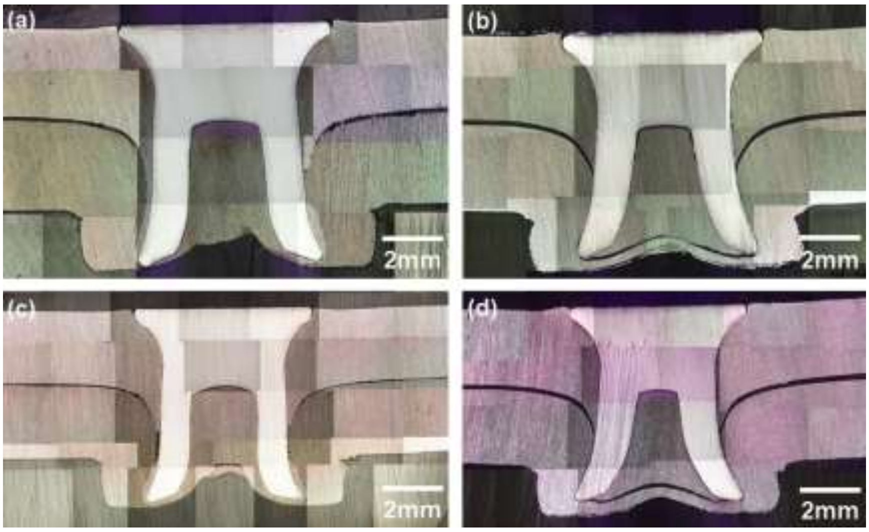

Fig. 7. Optical images of SPR sample: (a) cross-tension specimen of group 1, (b) lip-shear specimen of group 2, (c) cross-tension specimen of group 3, and (d) lip-shear specimen of group 4.

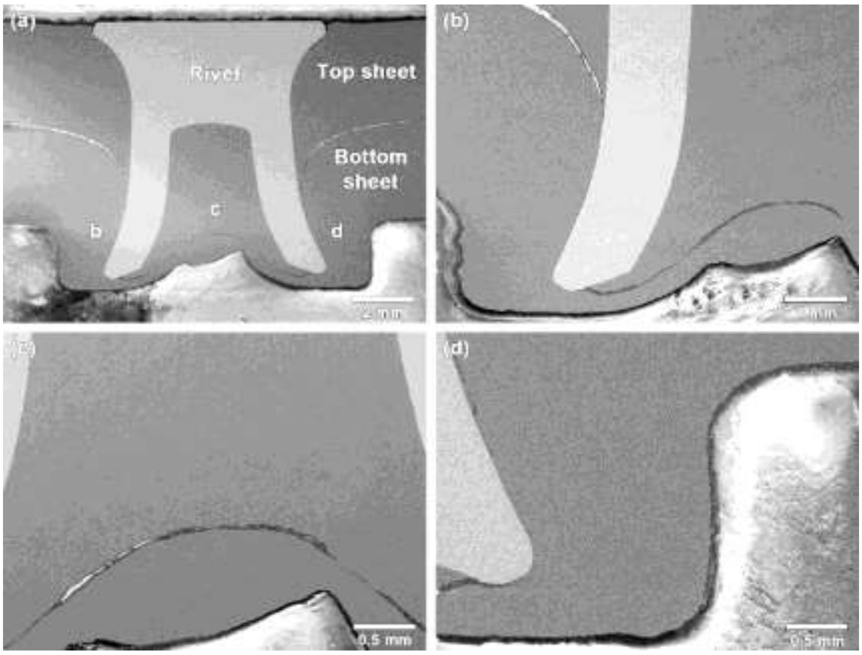

Fig. 8. SEM images of SPR sample: (a) cross-section view of SPR joint, (b) rivet flaring, (c) the center of the bottom button, and (d) the corner of the bottom button.

In spite of the known influence of those factors, the direct measurement of them in each process is a particularly difficult problem and therefore the quantification with an alternative method is quite attractive in industrial applications where time and cost are more meaningful. The load-displacement curve provides a window for comprehensively characterizing the metal deformation in the SPR process, which combines the various factors including of tool action and the time evolution of metal deformation resistance. The current study collected the load-displacement curves in the four groups of SPR specimen, as shown in Fig. 9. No significant difference is found in those curves which can also be divided into two stages according to the rivet flaring deformation: (a) stage I is the rivet piercing through the stacked sheets without significant deformation, (b) stage II is the large deformation resistance from the bottom mold forcing the rivet tail to flare. When the steel rivet is going to flare, a rapidly increasing of deformation resistance give a birth to a step on the load-displacement curve, as shown in Fig. 10, where d_0 and d_{max} is the distance of stage I and the total displacement of punch stroke in the riveting direction, respectively.

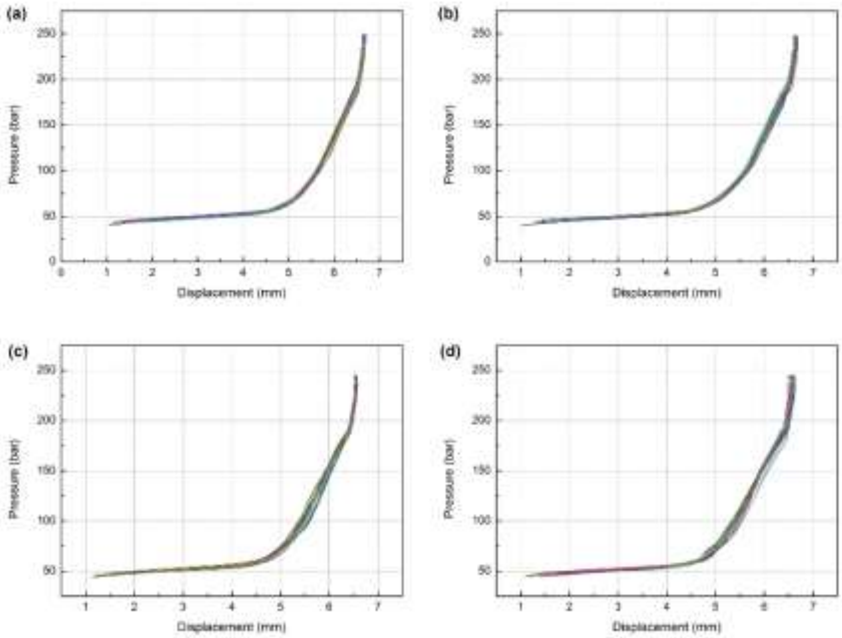

Fig. 9. Force-displacement curve of SPR processing: (a) cross-tension specimen of group 1, (b) lip-shear specimen of group 2, (c) cross-tension specimen of group 3, and (d) lip-shear specimen of group 4.

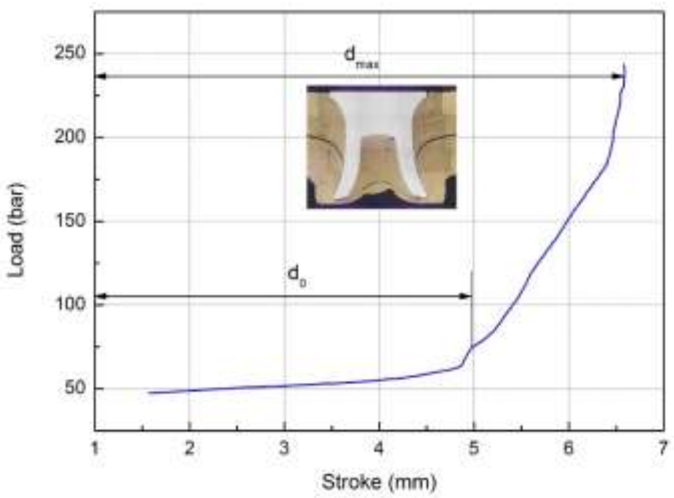

Fig. 10. The load-displacement curve of the SPR of two Al alloy sheets with a steel rivet.

3.3. SPR strength test results

Most of the current assessments on the SPR strength are cross-tension strength and lap-shear strength, which are also considered in this study. With the four groups of the SPR specimens, the destructive tests were implemented in the same testing conditions, where the failure models and strength results of the specimens were compared and discussed in the following contents.

Regardless of the coating on the sheets, the failure modes of those specimens can be divided into three categories (see Fig. 11): (a) failure mode I, the rivet tail pullout from the bottom sheet, (b) failure mode II, the rivet head pullout from the top sheet, (c) failure mode III, rivet failure. The failure of rivet (failure mode III), as reported by Haque and Durandet [42], is not found in the current study perhaps, which is due to the yield strength of the steel rivet utilized here is much larger than that of the stacked sheets.

Fig. 11. The tested SPR specimens: (a) cross-tension specimen of group 1, (b) lip-shear specimen of group 2, (c) cross-tension specimen of group 3, and (d) lip-shear specimen of group 4.

The failure mode I is the main mode observed in the cross-tension tests (group 1 and group 3) while the failure mode II is the main mode observed in the lap-shear tests (group 2 and group 4), as shown in Fig. 12.

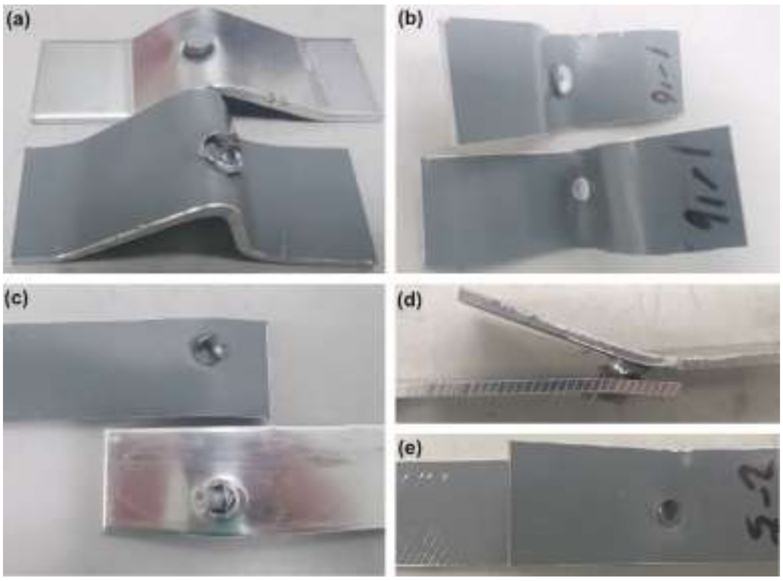

Fig. 12. The failure mode of the SPR specimens: (a,b) rivet head pullout (failure mode II) in cross-tension tests, (c) rivet tail pullout (failure mode I) in lip-shear test, (d,e) rivet pullout (failure mode III) in lip-shear tests.

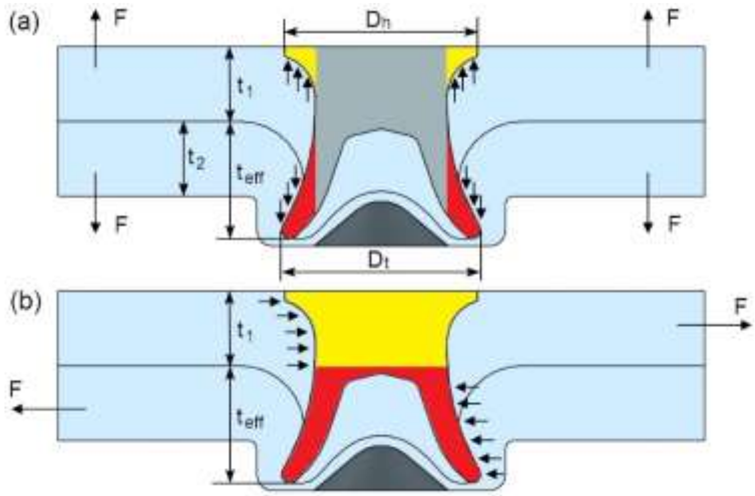

Fig. 13. The scheme of force distribution in the strength tests: (a) cross-tension test, (b) lap-shear test.

In the cross-tension test, the top sheet transfers the tensile stress to the rivet heat (yellow area in Fig. 13) along the vertical direction upwards and the bottom sheet transfer the tensile stress to the flared rivet tail (red area in Fig. 13) along the vertical direction downwards. Although the areas of the two parts in Fig. 13 (a) are similar, the riveted joint seems prefer to separate at the interface between the rivet head and the top sheet. To quantify the failure behavior, the pull-over strength of the rivet head can be calculated based on the BS 5950-5-1998 published by British Standard Institution [60] as follows:

$$P_V = 1.1 t_1 d_h p_y \tag{1}$$

where P_V is the normal pull-over strength, t_1 is the sheet thickness in contact with rivet head (mm), d_h is the diameter of rivet head (mm), p_y is the yield strength of the sheets. As an instance, considering a specimen in group 1 (see Fig. 13a), the pull-over strength of the rivet head in the SPR joint is $P_V = 1.1 t_1 D_h p_y$ = 1.1×2.5 mm×7.52 mm×120 MPa = 2481.6 N, and the pullout strength of the rivet tail is $P_V = 1.1 t_{\text{eff}} D_t p_y$ = 1.1×3.8 mm×7.12 mm×120 MPa = 3571.4 N. This proofs that the rivet tail has higher strength than the rivet head in the cross-tension tests (group 1 and 3), which leads to the pullout of rivet head (failure mode I).

In the lap-shear test (see Fig. 13b), the pullout strength can be similarly calculated by Eq. (1). As an instance, considering a specimen in group 2 (see Fig. 13b), the pull-over strength of the rivet head is $P_V = 1.1 t_3 D_h p_y$ = 1.1×5.5 mm×7.52 mm×120 MPa = 5459.5 N, and the pullout strength of the rivet tail is $P_V = 1.1 t_4 D_t p_y$ = 1.1×2.5 mm×7.12 mm×120 MPa = 2349.6 N. This proofs that the rivet head has higher strength than the rivet tail in the lap-shear tests (group 1 and 3), which leads to the pullout of rivet tail (failure mode II).

In the above calculation, a constant of 120 MPa utilized as the yield stress is inconsistent with the fact that the large deformation introduced work hardening can significantly improve the hardness at location therefore the yield strength of the material surrounding the rivet tail also increase in a linear proportion. As reported by Su, Lin, Lai and Pan [31], the hardness in the large deformation of the SPRed 6111-T4 aluminum sheet rises to 160 HV while the hardness of sheet matrix is only 85 HV. The microhardness of the SPRed AA5182-O joint reported by Ma, et al. [61] can rise to 136 HV, which is much greater than the hardness (79 HV) of the base metal. The hardness - yield stress linear relationship of Al alloy 7010 is reported by Tiryakioğlu, et al. [62] as Eq. (2):

$$\sigma_Y = 0.383H_V - 182.3 \tag{2}$$

where σ_Y is the yield stress of alloy (MPa), H_V is the Vickers hardness, and the scope is related to contact mechanics principles.

The strength of SPR joint is generally expressed by the maximum cross-tension force and maximum lap-shear force, both of which can be measured by the experimental tested force-displacement curve, as shown in Fig. 14. From the force-deformation curves in the cross-tension tests of group 1 and 3, the average values of the maximum cross-tension force are 3474.6 ± 211.5 MPa and 3326.7 ± 202.7 MPa, respectively. In the case of lap-shear tests of group 2 and 3, the average values of the maximum lap-shear force are 5690.4 ± 188.1 MPa and 6203.5 ± 336.0 MPa, respectively. A few abnormal test data are excluded from this statistic because these abnormal data will cause the statistical results to be much greater or lower than the normal level.

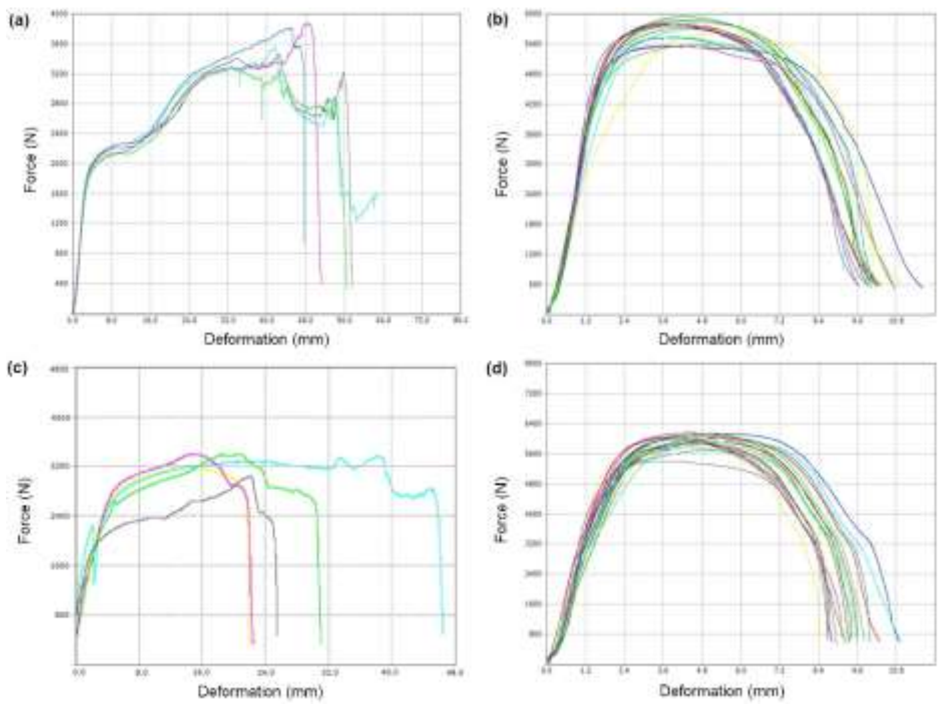

Fig. 14. Force-displacement curves: (a) cross-tension test of group 1, (b) lip-shear tests of group 2, (c) cross-tension tests of group 3, and (d) lip-shear tests of group 4.

Comparing the tendency of all the force-deformation curves, it is clear that the metal deformation process of the rivet tail pullout (failure mode I) in the lap-shear tests proceed more smoothly than that of the rivet heat pull-over (failure mode II) in cross-tension tests. As the desperation of the data displayed in Fig. 15, the average values of the lap-shear deformation in the group 2 and 4 are 10.21 ± 0.55 mm and 9.33 ± 0.84 mm, respectively. While the average values of the cross-tension deformation in group 1 and 3 are 49.77 ± 8.88 mm and 38.40 ± 13.75 mm, respectively. The linear fitting expressions of the cross-tension data are shown in Eqs. (3) - (6) where F_{CT1}, F_{CT2}, σ_{CT1}, σ_{CT2}, d is the maximum force in group 1, the maximum force in group 3, the maximum stress in group 1, the maximum stress in group 3 and the deformation (unit: mm), respectively. The values of R^2 of the four functions suggest the low linear properties of the cross-tension strength.

$$F_{CT1} = 3079.82 + 7.92d,\ R^2 = 0.1103 \tag{3}$$

$$F_{CT2} = 2810.50 + 11.38d,\ R^2 = 0.5072 \tag{4}$$

$$\sigma_{CT1} = 34.19 + 0.887d,\ R^2 = 0.1123 \tag{5}$$

$$\sigma_{CT2} = 31.23 + 0.126d,\ R^2 = 0.5077 \tag{6}$$

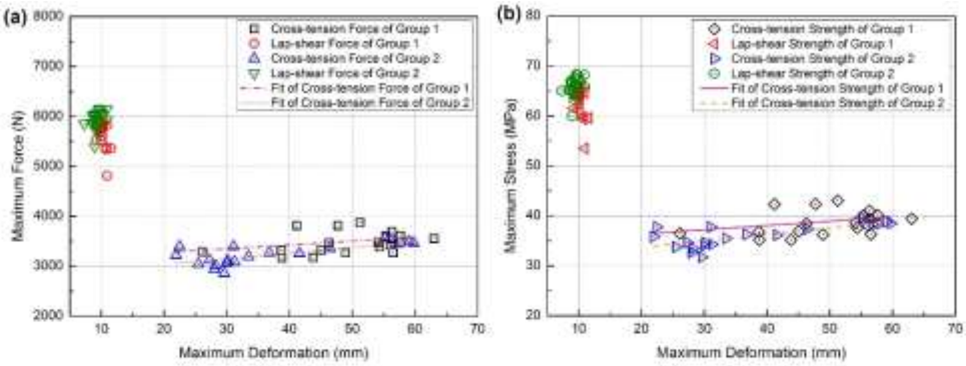

Fig. 15. The destructive test results: (a) force - deformation, and (b) stress - deformation.

3.4. General strength model of SPR

Notwithstanding the outstanding performances in the prediction of the SPR strength, numerical modeling has the disadvantages of low efficiency and poor operability. And the measurement of SPR strength by using experimental testing is destructive, time-delayed and cost-expensive, which is limited it application to the actual product. However, based on the numerical analysis and experimental data, establishing an empirical calculation model of SPR strength might overcome these limitations. As one of the most important mothed, the SPR strength model based on the rivet flaring has been well developed and verified in a broad range of sheet materials such as steel and aluminum alloy. Given the three component configuration as illustrated in Fig. 16, the rivet flaring Δ*d* is defined as the maximum deformation value of the rivet tail in one side, where D_h, D_t, t_{eff} are the rivet head diameter, deformed rivet tail diameter, and effective length of rivet in bottom sheet, respectively.

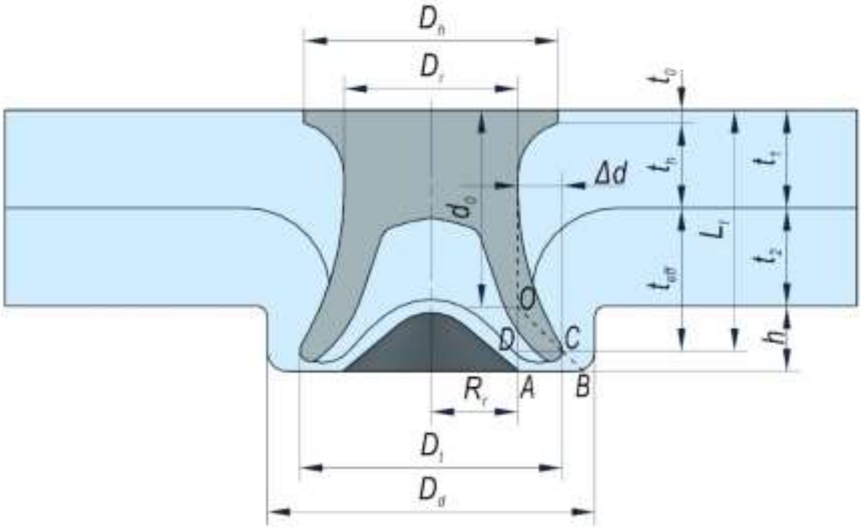

Fig. 16. Key parameters related to the metal deformation in the SPR.

According to the metal deformation during SPR process discussed in sections, the rivet piercing through a distance d_0 without significant deformation, therefore the major rivet flaring occurs in the stage II which starts from point O and completes at point C (see Fig. 16). The position of point C is of significantly important due to it correlated to the following terms: (a) the maximum diameter of the rivet flaring (D_t), (b) the maximum effective depth in the bottom sheet (t_{eff}), (c) the maximum effective length of the deformed rivet (L_t), (d) the diameter of the bottom die (D_d) which is the horizontal movement extreme of point C, and (e) the depth of bottom die (h) which is the vertical movement extreme of point C.

Constructing a right triangle △ODC, and extending the straight line OC to B which is located the bottom of the die, another right triangle △OAB is built as illustrated in Fig. 16, where the rivet flaring Δd equals to the length of CD. Due to the relationship of OD / OA =CD / AB, the magnitude of Δd is expressed as follows:

$$\Delta d = OD \cdot AB/OA \tag{7}$$

Considering the point O as the end point of the rivet deformation stage I (see Fig. 10), the vertical distance from point O to the top surface of rivet head is equal to d_0. Then OD, AB and OA can be calculated as follows:

$$OD = L_t - d_0 = C_1 \cdot d_{max} - d_0,\ 0 \leq C_1 \leq 1 \tag{8}$$

$$AB = C_2 \cdot (0.5D_d - R_r),\ 0 \leq C_2 \leq 1 \tag{9}$$

$$OA = t_1 + t_2 + h - d_0 \tag{10}$$

where L_t is the length of deformed rivet; C_1 is a empirical coenfficent related to the rivet length L ($0 \leq C_1 \leq 1$); d_{max} is the maxomum displacment of the punch which is measured from load-strokee curve; d_0 is the displacement of punch before rivet flaring; C_2 is a empirical coenfficent related to the rivet hardness ($0 \leq C_2 \leq 1$); D_d is the diameter of the bottom die; R_r, t_1, t_2, h is rivet radius, top sheet thickness, bottom sheet thickness, and the depth of bottom die, respectively.

The empirical expression of rivet flaring can be obtained by substituting Eqs. (8) - (10) into OD, AB, and OA in in Eq. (7):

$$\Delta d = \frac{(C_2 \cdot d_{max} - d_0) \cdot C_1 \cdot (0.5D_d - R_r)}{t_1 + t_2 + h - d_0} \tag{11}$$

An empirical estimator of failure mode II (rivet head pullout) is established Sun and Khaleel [44] by to calculate the cross-tension strength of SPR joint as follows:

$$F_h^T = \eta_h \beta_h t_1 \pi D_h \sigma_h \tag{12}$$

where F_h^T is rivet strength for rivet head pullout failure; η_h is empirical coefficient for the material degradation of sheet due to rivet piercing; β_h is empirical coefficient for head side sheet bending induced thickness reduction, $\beta_h = 1$ for $t_1 > 1.0$mm, $\beta_h \approx 0.7$ for $t_1 \leq 1.0$mm; $\pi \approx 3.14$; D_h is diameter of rivet head; σ_h is yield strength for head-side material.

Similarly, an empirical estimator of failure mode I (rivet tail pullout) is developed by Sun and Khaleel [44] to calculate the cross-tension strength of SPR joint as follows:

$$F_t^T = 0.7\eta_t\beta_t t_{eff}\pi D_t\sigma_t \quad (13)$$

where F_t^T is rivet strength for rivet tail pullout failure; η_t is empirical coefficient for the material degradation of tail-side sheet due to riveting, $\eta_t = 1$ for materials with elongation > 15%, $\eta_t = 0.5$ for extrusions or castings on tail end; β_t is empirical coefficient for tail side sheet bending induced thickness reduction, $\beta_t = 1$ for $t_2 > 1.0$ mm, $\beta_t \approx 0.7$ for $t_2 \leq 1.0$ mm; t_{eff} is effective material thickness on the tail-side; D_t is diameter of rivet flaring; σ_t is yield strength of base material in tail-side sheet.

The diameter of rivet flaring D_t and effective material thickness on the tail-side t_{eff} are calculated by Eqs. (14) and (15), respectively.

$$D_t = 2(R_r + \Delta d) \quad (14)$$

$$t_{eff} = t_2 + \frac{h-\Delta d}{2} \quad (15)$$

Then Eq. (13) has a new form as follows:

$$F_t^T = 0.7\eta_t\beta_t \cdot \left(t_2 - \frac{h-\Delta d}{2}\right)\pi \cdot 2(R_r + \Delta d) \cdot \sigma_t \quad (16)$$

Condiserating the balance of failure mode I and II, the rivet strength F_{CT} in cross-tension test can be expressed as follows:

$$F^T = \min\left(F_h^T, F_t^T\right) \quad (17)$$

There are two ways to calculate the lap-shear strength of SPR joint: (a) direct calculation of lap-shear strength, (b) indirect calculation from the cross-tension strength. As an instance, Haque and Durandet [42] analyzed the strength formula of blind rivet joint in Eurocode 9 (prEN1999-1-4) and proposed two empirical models to directly calculate the SPRed cross-tension strength of failure mode I and the lap-shear strength of failure mode II as follows:

$$F_{CT} = \alpha_{CT} \cdot \sigma_t \cdot \sqrt{D_t \cdot t_{eff}^3} \tag{13}$$

$$F_{LS} = \alpha_{LS} \cdot \sigma_t \cdot D_t \cdot t_{eff} \tag{18}$$

where F_{CT} is cross-tension strength; α_{CT} is empirical strength coefficient for cross-tension; F_{LS} is lap-shear strength; α_{LS} is empirical strength coefficient for lap-shear; t_{eff} is effective material thickness on the tail-side; D_t is diameter of rivet flaring; σ_t is yield strength of base material in tail-side sheet. Then the relationship is estiblished between cross-tension strength and lap-shear strength as follows:

$$F_{LS} = \left(\frac{\alpha_{LS}}{\alpha_{CT}} \cdot \sqrt{\frac{D_t}{t_{eff}}} \right) \cdot F_{CT} \tag{19}$$

Xie, Yan, Yu, Mu and Song [34] compared the strength formulas in Eurocode 9 (prEN1999-1-4), Eq. (13) proposed by Sun and Khaleel [44], Eq. (16) proposed by Haque and Durandet [42], China standard GB 50018-2002, British standard BS 5950-5-1998, North American standard AISI S100-2016 and Australia standard AS/NZS 4600-2005. They found that Eq. (13) and Eq. (16) have higher accuracy while the prediction results of Eurocode 9 is more conservative.

Considering the established models and the factors discussed above, general models for the strength prediction of SPR joint based rivet flaring is proposed here in terms of test method and failure mode as shown in Table 4.

Table 4 General strength models of SPR joint considering the different failure models.

	Rivet tail pullout (failure mode I)	Rivet head pullout (failure mode II)
Cross-tension strength	$F_t^{CT} = a_t t_{eff} D_t \sigma_t$ (20)*	$F_h^{CT} = a_h t_h D_h \sigma_h$ (21)
Lap-shear strength	$F_t^{LS} = b_t t_{eff} D_t \sigma_t$ (22)*	$F_h^{LS} = b_h t_1 D_h \sigma_h$ (23)

* where D_t, t_{eff} , and Δd are calculated by Eqs. (14), (15) and (11), respectively; empirical coefficients a_t, a_h, b_t, and b_h are obtained by experiment; t_h is the effective thickness of head-side material which is calculated with the thickness of head-side sheet t_1 and the highth of rivet head t_0 as Eq. (24):

$$t_h = \begin{cases} t_1 - t_0, & if \;\; rivet \;\; head \;\; in \;\; sheet \\ t_1, & if \;\; rivet \;\; head \;\; outside \;\; sheet \end{cases} \tag{24}$$

Condiserating the balance of failure mode I and II, the rivet strengths are expressed as Eqs. (25) and (26):

$$F_{CT} = \min\left(F_t^{CT}, F_h^{CT}\right) \tag{25}$$

$$F_{LS} = \min\left(F_t^{LS}, F_h^{LS}\right) \tag{26}$$

In the current study, the relationships between cross-tension strength (failure mode I or failure mode II) and lap-tension strength (failure mode I) are constructed with Eqs. (20), (21) and (22) as follows:

$$F_t^{LS} = \begin{cases} \frac{b_t}{a_t} \cdot F_t^{CT}, & if \;\; F_h^{CT} \geq F_t^{CT} \\ \frac{b_t t_{eff} D_t \sigma_t}{a_h t_1 D_h \sigma_h} \cdot F_h^{CT}, & if \;\; F_h^{CT} < F_t^{CT} \end{cases} \tag{27}$$

The Eq. (26) can be simplified as Eq. (27) when the SPR of similar sheets:

$$F_t^{LS} = \begin{cases} \frac{b_t}{a_t} \cdot F_t^{CT}, & if \;\; F_h^{CT} \geq F_t^{CT} \\ \frac{b_t}{a_h} \cdot \frac{t_{eff} D_t}{t_1 D_h} \cdot F_h^{CT}, & if \;\; F_h^{CT} < F_t^{CT} \end{cases} \tag{28}$$

The fist term in Eq. (28) is a constant depending on the coefficients in Eqs. (21) and (22). The second term in Eq. (28) is a variable depending on the geometric dimensions of rivet and sheets before and after deformation. The third terms in Eq. (28) is the obtained cross-tenison strength (failure mode II). The above strength models will be verified and discussed in the next section.

3.5. Verification of the general strength model

The above-mentioned models cannot be applied to quantify SPR joint strength before the following inlet data is well prepared: (a) geometric dimensions including of D_h, R_r, t_1, t_2, h, and D_d; (b) material properties σ_h and σ_t obtained by experimental test; (c) empirical coefficients C_l, C_l, α_h, and β_t; (d) punch displacements d_0 and $d_{\max}$. For the same batch of raw material, the data in group (a) and (b) can be assumed to be constant which depending on the suppliers' stringent quality control. The empirical coefficients in group (c) can be obtained by experimental method. The punch displacements can be measured from the load-displacement curve of SPR process. In addition, it also necessary to build an automated system with functions such as data transmission, data processing, strength calculation, data storage, and abnormal data feedback during each SPR process. The signal transmission in the proposed IIoT system is shown in the Fig. 17.

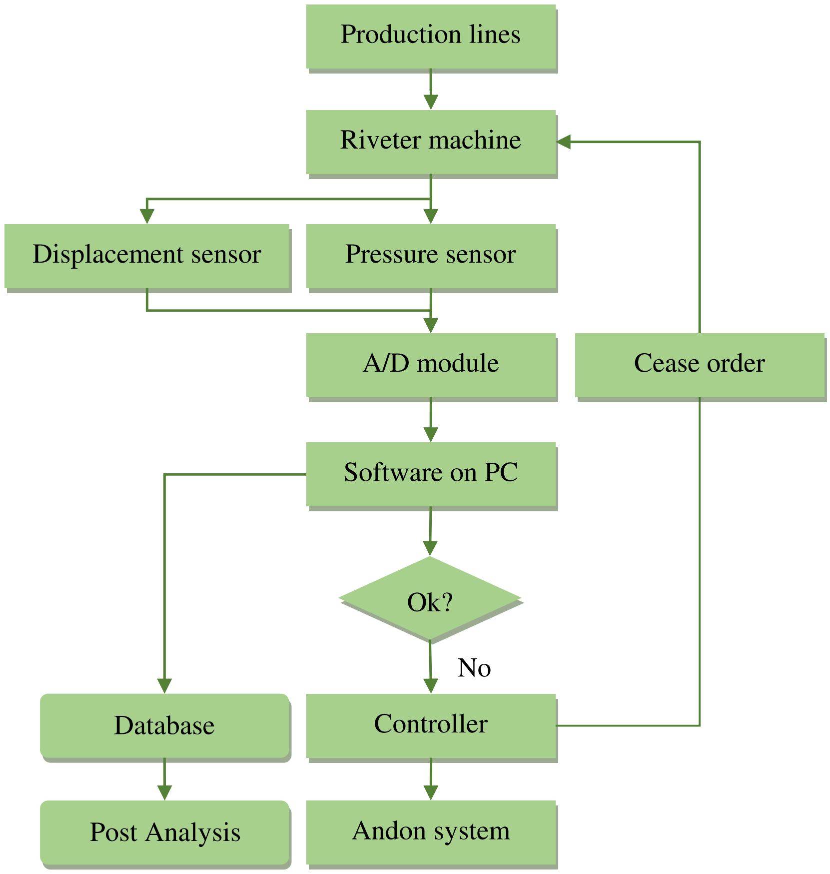

Fig. 17. Schematic diagram of the hardware and software in the proposed IIoT platform.

Example calculation is conducted by using the strength models (Eqs. 27 and 28) in section 3.4 and the 4 groups of specimens in destructive tests. Material parameters and empirical coefficients for calculation models of SPR joint strength are given in Table 5 and 6, respectively. The partial calculation results of the cross-tension strength and lap-shear strength are compared with the experimental results in Table 7 and 8, respectively.

Table 5 The material parameters of the SPR joint strength model.

t_1 (mm)	t_2 (mm)	t_0 (mm)	R_r (mm)	L (mm)	D_h (mm)	D_d (mm)	h (mm)	σ_t (MPa)	σ_h (MPa)
3	3	0.4	2.65	9	7.75	10	2	120	120

Table 6 The empirical coefficients of the SPR joint strength model.

C_1	C_2	η_t	β_t	a_h	b_t
0.53	0.9	0.55	1	1.4	2

Table 7 Comparison of the calculated results and experimental results of F_{CT}.

Group	Case	d_0 (mm)	$d_{\max}$ (mm)	Δd (mm)	D_t (mm)	t_{eff} (mm)	Measured F_{CT} (N)	Calculated F_{CT} (N)	Failure mode
1	1	5.300	6.628	0.307	5.913	3.847	3382.5	3299.8	I
1	2	5.016	6.677	0.415	6.129	3.793	3689.0	3372.3	I
1	3	5.568	6.609	0.195	5.689	3.903	3167.5	3221.1	I
1	4	5.544	6.626	0.213	5.726	3.894	3321.5	3234.0	I
1	5	5.219	6.631	0.335	5.970	3.832	3473.5	3319.3	I
2	6	5.207	6.564	0.312	5.925	3.844	3195.0	3604.0	I
2	7	5.253	6.572	0.300	5.900	3.850	3566.0	3594.7	I
2	8	5.348	6.569	0.265	5.830	3.868	3064.5	3568.2	I
2	9	5.336	6.537	0.256	5.812	3.872	3117.0	3561.3	I
2	10	5.307	6.532	0.264	5.829	3.868	3490.5	3567.9	I

Table 8 Comparison of the calculated results and experimental results of F_{LS}.

Group	Case	d_0 (mm)	$d_{\max}$ (mm)	Δd (mm)	D_t (mm)	t_{eff} (mm)	Measured F_{LS} (N)	Calculated F_{LS} (N)	Failure mode
3	1	5.249	6.667	0.340	5.980	3.830	5873.0	5496.6	I
3	2	5.252	6.665	0.338	5.976	3.831	5519.0	5494.7	I
3	3	5.249	6.616	0.319	5.939	3.840	5792.0	5473.6	I
3	4	5.336	6.655	0.306	5.911	3.847	5605.0	5458.0	I
3	5	5.373	6.636	0.285	5.869	3.858	5694.0	5433.9	I
4	6	5.201	6.557	0.312	5.924	3.844	6015.5	5465.0	I
4	7	5.158	6.552	0.324	5.948	3.838	5852.5	5478.6	I
4	8	5.237	6.521	0.285	5.870	3.858	5947.0	5434.2	I
4	9	5.084	6.521	0.335	5.971	3.832	6079.5	5491.7	I
4	10	5.230	6.538	0.294	5.889	3.853	5868.0	5445.2	I

The absolute errors of the predictions on the cross-tension strength and the lap-shear strength are shown in Fig. 18 (a) and (b), respectively. The average absolute errors of the 4 groups of data are 5.35%, 5.39%, 4.46%, and 7.50%, respectively. Comparing the errors of the strength prediction in Fig. 18 (a) and (b), established SPR strength models (Eqs. 27 and 28) perform sound in predicting the joint strengths (F_{CT} and F_{LS}) of the single-sided or double-sided coated sheets. The comparison of normalized predicted and measured strengths (F_{CT} and F_{LS}) is shown in Fig.18 (c) and (d). The premise of the above calculations is that the riveting is perfect. However, the abnormal situation that may actually occur is rivetless riveting, which can be filtered out from the normal SPR by mornitoring whether its load-displacement curve passes through circles A1 and A2, as shown in Fig. 19.

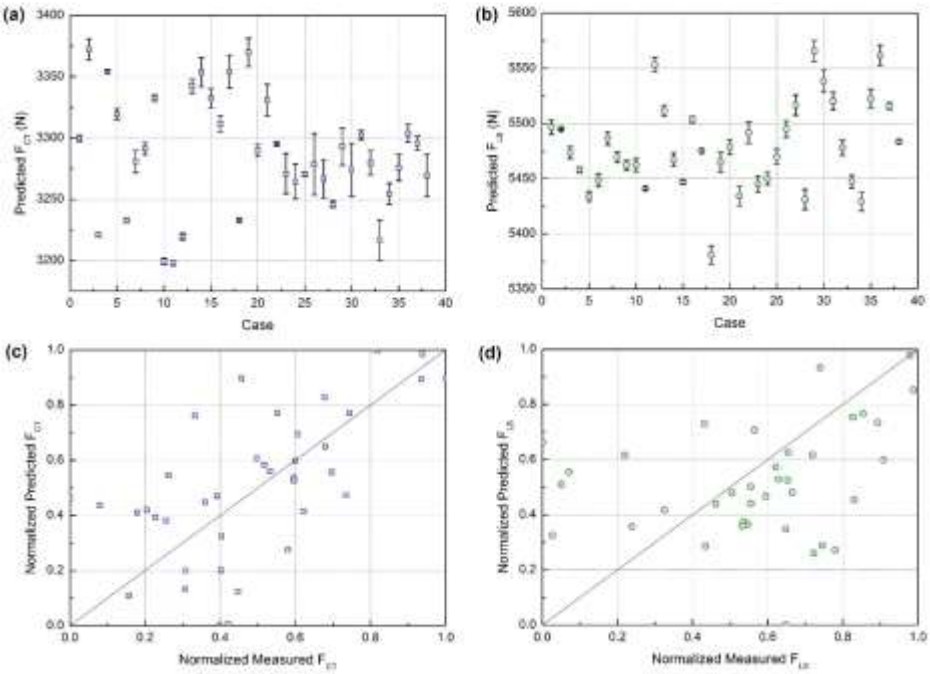

Fig. 18. Analysis on the prediction results: (a) predicted F_{CT} and error (%), (b) predicted F_{LS} and error (%), (c) linear relationship between predicted F_{CT} and measured F_{CT}, and (d) linear relationship between predicted F_{LS} and measured F_{LS}.

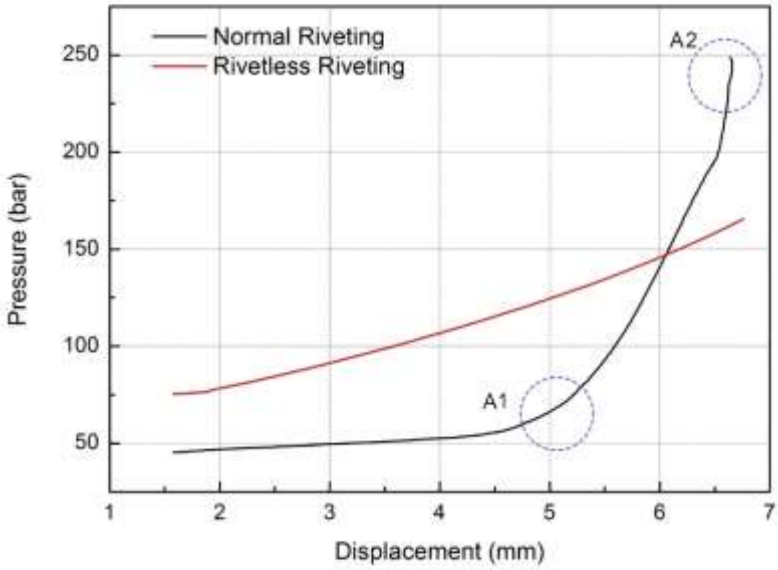

Fig. 19. Load-dislocation curves of rivetless riveting and normal riveting.

4. Conclusions

This study investigated the SPR process of two Al alloy sheets with one steel rivet in order to establish the general model of the cross-tension strength and lap-shear strength considering the different failure modes in practice. Conclusions are summarized as follows:

- Numerical simulation of finite element method coupled with metallography was utilized to reveal the cold metal deformation in SPR process. It is clear that the rivet travel through stacked sheets can be divided into two stages: (a) stage I is the rivet piercing stacked sheets and going into mold cavity; (b) stage II is the rivet flaring with the rivet severe deformation. The rivet flaring causes the punch load rapidly increasing, therefore it is possible to distinguish the starting and ending points of rivet flaring at the load-displacement curve of punch.
- The destructive tests of cross-tension and lap-shear specimens reveal the two failure modes of SPR joint in this study: rivet tail pullout (failure mode I), and rivet head pullout (failure mode II). The destructive test results provide credible evidences for the fact that the rivet

flaring is of significantly important to prevent the joint from debonding at the tail-side. The rivet flaring can be calculated based on the geometric deformation of rivet and stacked sheets, where the input parameters include of rivet dimensions (head diameter, radius, and length), mold size (depth and diameter), sheet thickness and so on. This study provided a new rivet flaring model in order to simplify the calculation procedure and improve the calculation accuracy.

- Base on the principle of rivet flaring, general strength models were proposed to calculate the cross-tension strength and lap-shear strength from the rivet flaring, material thickness, and material yield strength, regarding of the failure modes I and II. With the general strength models of SPR joint, it easy to obtain the relationship between the cross-tension strength and lap-shear strength, then calculating one of the strength value is possible if the other strength is known.
- The general strength models were utilized in industrial internet of things in order to predict the SPR quality in real time. The predicted results of SPR strength were compared with the experimental results to verify the general strength models of SPR. In the case of the SPR for one-side coated Al sheet and double-side coated sheet, the average absolute errors are 5.35% (cross-tension test) and 5.39% (lap-shear test). In the case of the SPR for two double-side coated sheets, the average absolute errors are 4.46% (cross-tension test) and 7.50% (lap-shear test).

Nomenclature:

Symbol	Unit	Parameter
t_0	mm	the highth of rivet head
t_1	mm	thickness of top sheet
t_2	mm	thickness of bottom sheet

L	mm	rivet length
D_h	mm	diameter of rivet head
R_r	mm	rivet radius
H	HV	rivet hardness
D_d	mm	diameter of flat die
h	mm	depth of flat die
t_{eff}	mm	effective length of rivet in bottom sheet
t_h	mm	effective thickness of head-side material
Dt	mm	diameter of deformed rivet
d_0	mm	punch displacement before rivet flaring
d_{max}	mm	maximum punch displacement
C_1	-	coefficient depends on rivet length ($0 \leq C1 \leq 1$)
C_2	-	coefficient depends on rivet hardness ($0 \leq C2 \leq 1$)
η_t	-	empirical coefficient of material degradation
β_t	-	empirical coefficient of sheet thickness reduction
σ_h	MPa	yield strength of heat-side sheet
σ_t	MPa	yield strength of tail-side sheet
Δd	mm	rivet flaring
α_{CT}	-	empirical coefficient for cross-tension
α_{LS}	-	empirical coefficient for lap-shear
a_t	-	empirical coefficient for cross-tension in failure mode I
a_h	-	empirical coefficient for cross-tension in failure mode II
b_t	-	empirical coefficient for lap-shear in failure mode I
b_h	-	empirical coefficient for lap-shear in failure mode II
F_t^{CT}	N	cross-tension strength in failure mode I
F_h^{CT}	N	cross-tension strength in failure mode II
F_t^{LS}	N	lap-shear strength in failure mode I
F_h^{LS}	N	lap-shear strength in failure mode II
F_{CT}	N	cross-tension strength
F_{LS}	N	lap-shear strength

Author contribution: All authors contributed to the study conception and design. Material preparation, data collection and analysis were performed by Yahui Liu, Zhiwang Zhu, Huipeng Yu, and Jun Wang. The first draft of the manuscript was written by Yahui Liu and all authors commented on previous versions of the manuscript. All authors read and approved the final manuscript.

Data availability: Not applicable.

Code availability: Not applicable.

Declarations

Ethics approval: The present manuscript contains an original research; it has not been published elsewhere, it has not been submitted simultaneously for publication elsewhere, and publication has been approved by the co-author.

Consent to participate: Not applicable.

Consent for publication: The present paper does not require any consent to publish since all the figures, tables, and text are original.

Conflict of interest: The authors declare no competing interests.

References

[1] Li D (2017) Influence of aluminium sheet surface modification on the self-piercing riveting process and the joint static lap shear strength. The International Journal of Advanced Manufacturing Technology 93: 2685-2695. https://doi.org/10.1007/s00170-017-0710-6

[2] Li D, Chrysanthou A, Patel I, Williams G (2017) Self-piercing riveting-a review. The International Journal of Advanced Manufacturing Technology 92: 1777-1824. https://doi.org/10.1007/s00170-017-0156-x

[3] Wu J, Chen C, Ouyang Y, Qin D, Li H (2021) Recent development of the novel riveting processes. The International Journal of Advanced Manufacturing Technology 117: 19-47. https://doi.org/10.1007/s00170-021-07689-w

[4] Han L, Chrysanthou A, Young K W (2007) Mechanical behaviour of self-piercing riveted multi-layer joints under different specimen configurations. Materials & Design 28: 2024-2033. https://doi.org/10.1016/j.matdes.2006.06.015

[5] He X, Wang Y, Lu Y, Zeng K, Gu F, Ball A (2015) Self-piercing riveting of similar and dissimilar titanium sheet materials. The International Journal of Advanced Manufacturing Technology 80: 2105-2115. https://doi.org/10.1007/s00170-015-7174-3

[6] Calabrese L, Bonaccorsi L, Proverbio E, Di Bella G, Borsellino C (2013) Durability on alternate immersion test of self-piercing riveting aluminium joint. Materials & Design 46: 849-856. https://doi.org/10.1016/j.matdes.2012.11.016

[7] He X, Zhao L, Deng C, Xing B, Gu F, Ball A (2015) Self-piercing riveting of similar and dissimilar metal sheets of aluminum alloy and copper alloy. Materials & Design (1980-2015) 65: 923-933. https://doi.org/10.1016/j.matdes.2014.10.002

[8] Xie Z, Yan W, Yu C, Mu T, Song L (2018) Experimental investigation of cold-formed steel shear walls with self-piercing riveted connections. Thin-Walled Structures 131: 1-15. https://doi.org/10.1016/j.tws.2018.06.028

[9] Zhao L, He X, Xing B, Zhang X, Cheng Q, Gu F, Ball A (2017) Fretting behavior of self-piercing riveted joints in titanium sheet materials. Journal of Materials Processing Technology 249: 246-254. https://doi.org/10.1016/j.jmatprotec.2017.06.016

[10] Rao H M, Kang J, Huff G, Avery K (2018) Impact of specimen configuration on fatigue properties of self-piercing riveted aluminum to carbon fiber reinforced polymer composite. International Journal of Fatigue 113: 11-22. https://doi.org/10.1016/j.ijfatigue.2018.03.031

[11] Gay A, Lefebvre F, Bergamo S, Valiorgue F, Chalandon P, Michel P, Bertrand P (2016) Fatigue performance of a self-piercing rivet joint between aluminum and glass fiber reinforced thermoplastic composite. International Journal of Fatigue 83: 127-134. https://doi.org/10.1016/j.ijfatigue.2015.10.004

[12] Han L, Chrysanthou A (2008) Evaluation of quality and behaviour of self-piercing riveted aluminium to high strength low alloy sheets with different surface coatings. Materials & Design 29: 458-468. https://doi.org/10.1016/j.matdes.2006.12.020

[13] Hoang N H, Porcaro R, Langseth M, Hanssen A G (2010) Self-piercing riveting connections using aluminium rivets. International Journal of Solids and Structures 47: 427-439. https://doi.org/10.1016/j.ijsolstr.2009.10.009

[14] Karathanasopoulos N, Pandya K S, Mohr D (2021) An experimental and numerical investigation of the role of rivet and die design on the self-piercing riveting joint characteristics of aluminum and steel sheets. Journal of Manufacturing Processes 69: 290-302. https://doi.org/10.1016/j.jmapro.2021.07.049

[15] Sun X, Khaleel M A (2007) Dynamic strength evaluations for self-piercing rivets and resistance spot welds joining similar and dissimilar metals. International Journal of Impact Engineering 34: 1668-1682. https://doi.org/10.1016/j.ijimpeng.2006.09.092

[16] Sun X, Stephens E, Khaleel M (2007) Fatigue behaviors of self-piercing rivets joining similar and dissimilar sheet metals. International Journal of Fatigue 29: 370-386. https://doi.org/10.1016/j.ijfatigue.2006.02.054

[17] Ma Y, Niu S, Liu H, Li Y, Ma N (2021) Microstructural evolution in friction self-piercing riveted aluminum alloy AA7075-T6 joints. Journal of Materials Science & Technology 82: 80-95. https://doi.org/10.1016/j.jmst.2020.12.023

[18] Ma Y, Yang B, Hu S, Shan H, Geng P, Li Y, Ma N (2022) Combined strengthening mechanism of solid-state bonding and mechanical interlocking in friction self-piercing riveted AA7075-T6 aluminum alloy joints. Journal of Materials Science & Technology 105: 109-121. https://doi.org/10.1016/j.jmst.2021.07.026

[19] Yang B, Shan H, Liang Y, Ma Y, Niu S, Zhu X, Li Y (2022) Effect of adhesive application on friction self-piercing riveting (F-SPR) process of AA7075-T6 aluminum alloy. Journal of Materials Processing Technology 299: 117336. https://doi.org/10.1016/j.jmatprotec.2021.117336

[20] Yang B, Ma Y, Shan H, Niu S, Li Y (2021) Friction self-piercing riveting (F-SPR) of aluminum alloy to magnesium alloy using a flat die. Journal of Magnesium and Alloys. https://doi.org/10.1016/j.jma.2020.12.016

[21] Ma Y, Niu S, Shan H, Li Y, Ma N (2020) Impact of Stack Orientation on Self-Piercing Riveted and Friction Self-Piercing Riveted Aluminum Alloy and Magnesium Alloy Joints. Automotive Innovation 3: 242-249. https://doi.org/10.1007/s42154-020-00108-y

[22] Ying L, Gao T, Dai M, Hu P, Dai J (2021) Towards joinability of thermal self-piercing riveting for AA7075-T6 aluminum alloy sheets under quasi-static loading conditions. International Journal of Mechanical Sciences 189: 105978. https://doi.org/10.1016/j.ijmecsci.2020.105978

[23] Han D, Yang K, Meschut G (2021) Mechanical joining of glass fibre reinforced polymer (GFRP) through an innovative solid self-piercing rivet. Journal of Materials Processing Technology 296: 117182. https://doi.org/10.1016/j.jmatprotec.2021.117182

[24] Jiang H, Gao S, Li G, Cui J (2019) Structural design of half hollow rivet for electromagnetic self-piercing riveting process of dissimilar materials. Materials & Design 183: 108141. https://doi.org/10.1016/j.matdes.2019.108141

[25] Danyo M W, Self-piercing riveting (SPR) in the automotive industry: an overview, 2014, pp. 171-180.

[26] Wang J, Zhang G, Zheng X, Li J, Li X, Zhu W, Yanagimoto J (2021) A self-piercing riveting method for joining of continuous carbon fiber reinforced composite and aluminum alloy sheets. Composite Structures 259: 113219. https://doi.org/10.1016/j.compstruct.2020.113219

[27] Karim M A, Bae J-H, Kam D-H, Kim C, Choi W-H, Park Y-D (2020) Assessment of rivet coating corrosion effect on strength degradation of CFRP/aluminum self-piercing riveted joints. Surface and Coatings Technology 393: 125726. https://doi.org/10.1016/j.surfcoat.2020.125726

[28] Kyoung-Yun Kim, Jaemun Sim, Noor-E Jannat, Fahim Ahmed, Ameri S (2019) Challenges in riveting quality prediction: a literature survey. Procedia Manufacturing 1143–1150. https://doi.org/

[29] Porcaro R, Hanssen A G, Langseth M, Aalberg A (2006) Self-piercing riveting process: An experimental and numerical investigation. Journal of Materials Processing Technology 171: 10-20. https://doi.org/10.1016/j.jmatprotec.2005.05.048

[30] Lou M, Li Y, Wang Y, Wang B, Lai X (2014) Influence of resistance heating on self-piercing riveted dissimilar joints of AA6061-T6 and galvanized DP590. Journal of Materials Processing Technology 214: 2119-2126. https://doi.org/10.1016/j.jmatprotec.2014.03.006

[31] Su Z-M, Lin P-C, Lai W-J, Pan J (2015) Fatigue analyses of self-piercing rivets and clinch joints in lap-shear specimens of aluminum sheets. International Journal of Fatigue 72: 53-65. https://doi.org/10.1016/j.ijfatigue.2014.09.022

[32] Zhang X, He X, Wei W, Lu J, Zeng K (2020) Fatigue characterization and crack propagation mechanism of self-piercing riveted joints in titanium plates. International Journal of Fatigue 134: 105465. https://doi.org/10.1016/j.ijfatigue.2019.105465

[33] Yan W, Xie Z, Yu C, Song L, He H (2017) Experimental investigation and design method for the shear strength of self-piercing rivet connections in thin-walled steel structures. Journal of Constructional Steel Research 133: 231-240. https://doi.org/10.1016/j.jcsr.2017.02.022

[34] Xie Z, Yan W, Yu C, Mu T, Song L (2018) Tensile capacity of self-piercing rivet connections in thin-walled steel structures. Journal of Constructional Steel Research 144: 211-220. https://doi.org/10.1016/j.jcsr.2018.01.022

[35] Kang S-H, Kim H-K (2015) Fatigue strength evaluation of self-piercing riveted Al-5052 joints under different specimen configurations. International Journal of Fatigue 80: 58-68. https://doi.org/10.1016/j.ijfatigue.2015.05.003

[36] Wu G, Li D, Lai W-J, Shi Y, Kang H, Peng Y, Su X (2021) Fatigue behaviors and mechanism-based life evaluation on SPR-bonded aluminum joint. International Journal of Fatigue 142: 105948. https://doi.org/10.1016/j.ijfatigue.2020.105948

[37] Presse J, Künkler B, Michler T (2021) Stress-based approach for fatigue life calculation of multi-material connections hybrid joined by self-piercing rivets and adhesive. Thin-Walled Structures 159: 107192. https://doi.org/10.1016/j.tws.2020.107192

[38] Chen Y K, Han L, Chrysanthou A, O'Sullivan J M (2003) Fretting wear in self-piercing riveted aluminium alloy sheet. Wear 255: 1463-1470. https://doi.org/10.1016/s0043-1648(03)00274-6

[39] Kotadia H R, Rahnama A, Sohn I R, Kim J, Sridhar S (2019) Performance of dissimilar metal Self-Piercing Riveting (SPR) joint and coating behaviour under corrosive environment. Journal of Manufacturing Processes 39: 259-270. https://doi.org/10.1016/j.jmapro.2019.02.024

[40] Liu Y, Li H, Zhao H, Liu X (2019) Effects of the die parameters on the self-piercing riveting process. The International Journal of Advanced Manufacturing Technology 105: 3353-3368. https://doi.org/10.1007/s00170-019-04567-4

[41] Zhao L, He X, Xing B, Lu Y, Gu F, Ball A (2015) Influence of sheet thickness on fatigue behavior and fretting of self-piercing riveted joints in aluminum alloy 5052. Materials & Design 87: 1010-1017. https://doi.org/10.1016/j.matdes.2015.08.121

[42] Haque R, Durandet Y (2016) Strength prediction of self-pierce riveted joint in cross-tension and lap-shear. Materials & Design 108: 666-678. https://doi.org/10.1016/j.matdes.2016.07.029

[43] Sun X, Khaleel M A (2005) Performance Optimization of Self-Piercing Rivets Through Analytical Rivet Strength Estimation. Journal of Manufacturing Processes 7: 83-93. https://doi.org/10.1016/s1526-6125(05)70085-2

[44] Sun X, Khaleel M A (2005) Strength estimation of self-piercing rivets using lower bound limit load analysis. Science and Technology of Welding and Joining 10: 624-635. https://doi.org/10.1179/174329305x57491

[45] Karim M A, Jeong T-E, Noh W, Park K-Y, Kam D-H, Kim C, Nam D-G, Jung H, Park Y-D (2020) Joint quality of self-piercing riveting (SPR) and mechanical behavior under the frictional effect of various rivet coatings. Journal of Manufacturing Processes 58: 466-477. https://doi.org/10.1016/j.jmapro.2020.08.038

[46] Zhao H, Han L, Liu Y, Liu X (2021) Modelling and interaction analysis of the self-pierce riveting process using regression analysis and FEA. The International Journal of Advanced Manufacturing Technology 113: 159-176. https://doi.org/10.1007/s00170-020-06519-9

[47] Wang D, Kong D, Xie C, Li S, Zong L (2022) Study on the effect of rivet die parameters on joint quality of self-piercing riveting employed 3D modeling and MCDM method. The International Journal of Advanced Manufacturing Technology 119: 8227-8241. https://doi.org/10.1007/s00170-022-08759-3

[48] He X, Xing B, Zeng K, Gu F, Ball A (2013) Numerical and experimental investigations of self-piercing riveting. The International Journal of Advanced Manufacturing Technology 69: 715-721. https://doi.org/10.1007/s00170-013-5072-0

[49] Moraes J F C, Jordon J B, Su X, Barkey M E, Jiang C, Ilieva E (2019) Effect of process deformation history on mechanical performance of AM60B to AA6082 self-pierce riveted joints. Engineering Fracture Mechanics 209: 92-104. https://doi.org/10.1016/j.engfracmech.2018.12.020

[50] Du Z, Duan L, Jing L, Cheng A, He Z (2021) Numerical simulation and parametric study on self-piercing riveting process of aluminium–steel hybrid sheets. Thin-Walled Structures 164: 107872. https://doi.org/10.1016/j.tws.2021.107872

[51] Casalino G, Rotondo A, Ludovico A (2008) On the numerical modelling of the multiphysics self piercing riveting process based on the finite element technique. Advances in Engineering Software 39: 787-795. https://doi.org/10.1016/j.advengsoft.2007.12.002

[52] Carandente M, Dashwood R J, Masters I G, Han L (2016) Improvements in numerical simulation of the SPR process using a thermo-mechanical finite element analysis. Journal of Materials Processing Technology 236: 148-161. https://doi.org/10.1016/j.jmatprotec.2016.05.001

[53] Lukas Potgorschek J D, Florian Hönsch, Christof Sommitsch, Stefan Kaufmann (2020) Numerical simulation of hybrid joining processes: self-piercing riveting combined with adhesive bonding. 23rd International Conference on Material Forming (ESAFORM 2020), pp. 413-418.

[54] Hönsch F, Domitner J, Sommitsch C, Götzinger B (2020) Modeling the Failure Behavior of Self-Piercing Riveting Joints of 6xxx Aluminum Alloy. Journal of Materials Engineering and Performance 29: 4888-4897. https://doi.org/10.1007/s11665-020-04894-8

[55] Haque R, Williams N S, Blacket S E, Durandet Y (2015) A simple but effective model for characterizing SPR joints in steel sheet. Journal of Materials Processing Technology 223: 225-231. https://doi.org/10.1016/j.jmatprotec.2015.04.006

[56] Kim C, Min K M, Choi H, Kim H J, Lee M-G (2021) Development of analytical strength estimator for self-piercing rivet joints through observation of finite element simulations.

International Journal of Mechanical Sciences 202-203: 106499. https://doi.org/10.1016/j.ijmecsci.2021.106499

[57] Porcaro R, Hanssen A G, Langseth M, Aalberg A (2006) An experimental investigation on the behaviour of self-piercing riveted connections in aluminium alloy AA6060. International Journal of Crashworthiness 11: 397-417. https://doi.org/10.1533/ijcr.2005.0108

[58] He X, Pearson I, Young K (2008) Self-pierce riveting for sheet materials: State of the art. Journal of Materials Processing Technology 199: 27-36. https://doi.org/10.1016/j.jmatprotec.2007.10.071

[59] Hoang N H, Hanssen A G, Langseth M, Porcaro R (2012) Structural behaviour of aluminium self-piercing riveted joints: An experimental and numerical investigation. International Journal of Solids and Structures 49: 3211-3223. https://doi.org/10.1016/j.ijsolstr.2012.05.039

[60] Institution B S (1998) BS 5950-5:1988, Structural Use of Steelwork in Building: Part 5: Code of Practice for Design of Cold Formed Thin Gauge Sections. British Standard Institution, London.

[61] Ma Y, Shan H, Niu S, Li Y, Lin Z, Ma N (2020) A Comparative Study of Friction Self-Piercing Riveting and Self-Piercing Riveting of Aluminum Alloy AA5182-O. Engineering. https://doi.org/10.1016/j.eng.2020.06.015

[62] Tiryakioğlu M, Robinson J S, Salazar-Guapuriche M A, Zhao Y Y, Eason P D (2015) Hardness–strength relationships in the aluminum alloy 7010. Materials Science and Engineering: A 631: 196-200. https://doi.org/10.1016/j.msea.2015.02.049

Caption of Tables and Figures

Fig. 1. The SPR schematic diagram of aluminum alloy sheet: (a) preparation, (b) forming, (c) demolding.

Fig. 2. The SPR device utilized for the Al sheet riveting.

Fig. 3. The SPR specimens of destructive tests: (a) cross-tension specimen of group 1, (b) lip-shear specimen of group 1, (c) cross-tension specimen of group 3, and (d) lip-shear specimen of group 4.

Fig. 4. The 2D axis symmetric FE model of SPR for the Al sheet and steel rivet.

Fig. 5. FE simulation results of Mises stress at the different punch stroke: (a) 5%, (b) 25%, (c) 45%, (d) 65%, (e) 85%, and (f) 100%.

Fig. 6. The predicted displacement field of SPR joint in (a) total magnitude, (b) X axis direction, and (c) Y axis direction.

ig. 7. Optical images of SPR sample: (a) cross-tension specimen of group 1, (b) lip-shear specimen of group 2, (c) cross-tension specimen of group 3, and (d) lip-shear specimen of group 4.

Fig. 8. SEM images of SPR sample: (a) cross-section view of SPR joint, (b) rivet flaring, (c) the center of the bottom button, and (d) the corner of the bottom button.

Fig. 9. Force-displacement curve of SPR processing: (a) cross-tension specimen of group 1, (b) lip-shear specimen of group 2, (c) cross-tension specimen of group 3, and (d) lip-shear specimen of group 4.

Fig. 10. The load-displacement curve of the SPR of two Al alloy sheets with a steel rivet.

Fig. 11. The tested SPR specimens: (a) cross-tension specimen of group 1, (b) lip-shear specimen of group 2, (c) cross-tension specimen of group 3, and (d) lip-shear specimen of group 4.

Fig. 12. The failure mode of the SPR specimens: (a,b) rivet head pullout (failure mode II) in cross-tension tests, (c) rivet tail pullout (failure mode I) in lip-shear test, (d,e) rivet pullout (failure mode III) in lip-shear tests.

Fig. 13. The scheme of force distribution in the strength tests: (a) cross-tension test, (b) lap-shear test.

Fig. 14. Force-displacement curves: (a) cross-tension test of group 1, (b) lip-shear tests of group 2, (c) cross-tension tests of group 3, and (d) lip-shear tests of group 4.

Fig. 15. The destructive test results: (a) force - deformation, and (b) stress - deformation.

Fig. 16. Key parameters related to the metal deformation in the SPR.

Fig. 17. Schematic diagram of the hardware and software in the proposed IIoT platform.

Fig. 18. Analysis on the prediction results: (a) predicted F_{CT} and error (%), (b) predicted F_{LS} and error (%), (c) linear relationship between predicted F_{CT} and measured F_{CT}, and (d) linear relationship between predicted F_{LS} and measured F_{LS}.

Fig. 19. Load-dislocation curves of rivetless riveting and normal riveting.

Table 1 Chemical compositions of Aluminum 6063-T5.

Table 2 Chemical compositions of 37Cr4 steel.

Table 3 The mechanical properties of Al alloy 6063-T5 and 37Cr4 steel.

Table 4 General strength models of SPR joint considering the different failure models.

Table 5 The material parameters of the SPR joint strength model.

Table 6 The empirical coefficients of the SPR joint strength model.

Table 7 Comparison of the calculated results and experimental results of F_{CT}.

Table 8 Comparison of the calculated results and experimental results of F_{LS}.